UPPSALA
UNIVERSITET

Digital Comprehensive Summaries of Uppsala Dissertations from the Faculty of Science and Technology 710

X-ray Absorption Spectroscopy on Nano-Magnet Arrays and Thin Films

Magnetism and Structure

ANDREAS PERSSON

ACTA
UNIVERSITATIS
UPSALIENSIS
UPPSALA
2010

ISSN 1651-6214
ISBN 978-91-554-7712-7
urn:nbn:se:uu:diva-112824

Dissertation presented at Uppsala University to be publicly examined in Häggsalen, Ångströmlaboratoriet, Lägerhyddsvägen 1, Uppsala, Friday, March 5, 2010 at 10:15 for the degree of Doctor of Philosophy. The examination will be conducted in English.

Abstract
Persson, A. 2010. X-ray Absorption Spectroscopy on Nano-Magnet Arrays and Thin Films. Magnetism and Structure. Acta Universitatis Upsaliensis. *Digital Comprehensive Summaries of Uppsala Dissertations from the Faculty of Science and Technology* 710. 61 pp. Uppsala. ISBN 978-91-554-7712-7.

The magnetic and structural properties of nano magnet arrays and ferromagnetic thin films are investigated. Circular x-rays are used and extensive use is made in this Thesis of the X-ray Magnetic Circular Dichroism (XMCD) technique. By means of the XMCD magneto-optic sum rules the values of the orbital and spin moments are determined. In the case of the nano magnet arrays studied, the XMCD technique is used in a spatially resolved mode using Photo Electron Emission Microscopy (PEEM) after circular light excitation. The Extended X-ray Absorption Fine Structure (EXAFS) is studied in both the Co K- and L-edges.

In situ Co L-edge X-ray XMCD spectroscopy measurements are presented, in combination with spectro-microscopy results, on Co/Pt and Co/Au based nano-dot arrays, of typical dot lateral size 250×100 nm^2, on self organized $Si_{0.5}Ge_{0.5}$. The Co is only a few atomic layers thick. The dot arrays display a high degree of lateral order and the individual dots, in several cases, exhibit a stable magnetic moment at 300 K. It is found possible to characterize the spin reorientation of these dot arrays. For both systems the in- versus out-of-plane orbital moment anisotropy, is not always related with an out-of-plane magnetization and the occurrence of a spin reorientation. By performing Co K-edge EXAFS measurements the local atomic structure around the Co atoms is characterized. The feasibility of a high precision quantitative structural analysis of L-EXAFS is studied on the system Au/Co/Au/W(110). The spin reorientation transition is studied as a function of the Co thickness and Au cap thickness. The L-edge EXAFS indicates that this reorientation is correlated to a lattice expansion in the perpendicular direction.

High precision angle dependent XMCD work is performed on a high temperature exchange bias system. Pinned or frozen magnetic moments are studied within an exchange biased NiFe ferromagnet at the NiFe/FeMn, ferromagnet/antiferromagnet interface by XMCD and complemented by x-ray resonant reflectivity experiments, at the Ni, Fe and Mn L-edges. The Mn L-edge XMCD MnSb and of (Ga, Mn)As layers modified by high temperature annealing is studied. For MnSb an enhanced value is obtained versus theoretical calculations. This result can be explained by means of the enhanced surface to volume ratio for the samples studied. For (Ga, Mn)As differences are found in the local environment of the Mn atoms upon annealing.

Keywords: self organization, nano-magnet, xmcd, exafs, peem, magnetism

Andreas Persson, Department of Physics and Materials Science, Surface and Interface Science, Box 530, Uppsala University, SE-75121 Uppsala, Sweden

ISSN 1651-6214
ISBN 978-91-554-7712-7
urn:nbn:se:uu:diva-112824 (http://urn.kb.se/resolve?urn=urn:nbn:se:uu:diva-112824)

To my parents and sister

List of Papers

This thesis is based on the following papers. Reprints were made with permission from the publishers.

I **Nanomagnet array and method of forming the same**
C. Teichert, C. Hofer, J. J. de Miguel, M. Á. Niño, N. Mikuszeit, E. Jiménez, J. Camarero, R. Miranda, D. Arvanitis, L. Gridneva, A. Persson, T. Bobek, and K. Heinrich
European patent office, 05.11.2008 Bulletin 2008/45

II **Experimental investigation of the spin reorientation of Co/Au based magnetic nanodot arrays**
L. Gridneva, A. Persson, M. Á. Niño, J. Camarero, J. J. de Miguel, R. Miranda, C. Hofer, C. Teichert, T. Bobek, A. Locatelli, S. Heun, S. Carlsson, and D. Arvanitis
Physical Review B (Condensed Matter and Materials Physics), **77**, 104425, 1 March 2008

III **On the spin reorientation of ordered magnetic nano-dot arrays: Pt/Co/Pt versus Au/Co/Au**
A. Persson, L. Gridneva, M. Á. Niño, J. Camarero, J. J. de Miguel, R. Miranda, C. Hofer, C. Teichert, T. Bobek, A. Locatelli, and D. Arvanitis
(In manuscript)

IV **Correlation of magnetism and structure for ultra thin Au/Co/Au films: evidence for magnetoelastic effects**
M. Sakamaki, T. Konishi, A. Persson, C. Andersson, O. Karis, D. Arvanitis, H. Rossner, and E. Holub-Krappe
Journal of Physics: Conference Series **190**, 012113 (2009)

V **Direct observation of frozen moments in the NiFe/FeMn exchange bias system**
J. Mohanty, A. Persson, D. Arvanitis, K. Temst, and C. Van Haesendonck
Submitted to Physical Review Letters

VI **XANES Studies of Mn K and $L_{3,2}$ Edges in the (Ga, Mn) As Layers Modified by High Temperature Annealing**
A. Wolska, K. Lawniczak-Jablonska, M.T. Klepka, R. Jakiela, J. Sadowski, I.N. Demchenko, E. Holub-Krappe, A. Persson, and D. Arvanitis
Acta Physica Polonica A, **114**, 357 (2008)

VII **Structural and magnetic properties of the molecular beam epitaxy grown MnSb layers on GaAs substrates**
K. Lawniczak-Jablonska, A. Wolska, J. Bak-Misiuk, E. Dynowska, P. Romanowski, J.Z. Domagala, R. Minikayev, D. Wasik, M.T. Klepka, J. Sadowski, A. Barcz, P. Dluzewski, S. Kret, A. Twardowski, M. Kamińska, A. Persson, D. Arvanitis, E. Holub-Krappe, and A. Kwiatkowski
Journal of Applied Physics, **106**, 083524 (2009)

Comments on my own participation

Experimental physics contains many facets including instrumentation development, service of experimental equipment, sample preparation, carrying through the measurements and finally analyzing and presenting the data for the scientific community. The work contained in the publications included in this Thesis is done by the contribution of several people belonging to outside groups, in collaboration. In the work presented in this Thesis, my role has been more active in the later sample analysis steps, to carry through the experimental work at MAX-lab and HASYLAB and to extract the physics out of the experimental data.

Been stationed in Lund, at MAX-lab, for several years, I have been responsible for the servicing of the experimental equipment I used at MAX-lab in coordination with the MAX-lab staff. I have introduced this equipment to several outside user groups. I have focused on the use of XAS and XMCD as these techniques yield the most relevant information for the investigated samples in the context of the other analysis tools used by the external collaborations. I have introduced our partners to the data analysis procedures, specific to XMCD. I have participated in the early commissioning of the new I1011 beamline and its associated equipment, the so called 3T and the 1T octupole end stations. Unfortunately, due to problems with some mechanical parts of the cPGM monochromator at I1011, I have not been able to include I1011 data in this Thesis.

My contribution in the published work is to some extent reflected by my position in the author list. Given the fact that several groups were collaborating, also an Institution block logic was often applied, influencing also the order of the authors.

Contents

1. Populärvetenskaplig sammanfattning

Uppfinningen av magnetiska lagringsenheter har haft en stor inverkan på ljud, video och datorer. En av de stora motiveringarna för att bedriva forskning på detta område är för att kunna ändra riktningen av magnetiseringen från i planet till ut ur planet och för att kunna få högre lagringskapacitet. Magnetiska nanopartiklar består oftast av magnetiska material så som järn, kobolt och nickel som kan manipuleras av magnetiska fält. Ferromagnetiska material består av små domäner, se Fig. 1.1, där varje domän innehåller väldigt många atomer, där varje atom är som en liten miniatyrmagnet. I ett ferromagnetiskt material kopplar alla de små atomära magneterna ihop sig till samma riktning i varje domän. Den magnetiska riktningen varierar från domän till domän, men det som gör att ferromagnetiska material är användbara är att alla domäner rätar upp sig under ett externt magnetisk fält även efter det att fältet är avstängt. Varför bär sig varje atom åt som en magnet? Ja det beror på att magnetfält uppstår då elektriska laddningar rör sig. En atom består av en positiv kärna och en mängd elektroner som rör sig runt kärnan. Denna rörelse kan ge strömmar som resulterar i ett bidrag till att atomen blir en magnet. På forskarspråk säger vi att atomens magnetiska moment har ett orbitalbidrag från elektronernas rörelse runt kärnan. Men elektronerna har en frihetsgrad till som fungerar som om de snurrar kring sin egen axel. Detta ger ytterligare ett bidrag till atomens magnetism som vi på forskarspråk kallas spinmomentet.

En dators hårddisk till exempel utnyttjar ferromagnetiska tunna filmer för informationenslagring. De magnetiska momenten i de olika domänerna är tvingade att arrangera sig efter det magnetiska fältet som produceras av läs huvudet i en hårddisk. Ett problem är dock att ett ferromagnetisk material som järn inte är stabilt, pågrund av anisotropin. För att lösa det problemet så använder man sig av ett antiferromagnetisk lager för att få en växelverkan med det ferromagnetiska lagret och på så sätt få stabil magnetisering. Eftersom magnetiseringen i de enskilda magnetiska domänerna är stabil kommer materialet ihåg informationen som har lagrats. Forskningen som jag har utfört kan användas för att undersäka magnetiska material för framtida datalagringsenheter. Genom att undersöka de magnetiska och strukturella egenskaperna hos filmer och magnetiska nanopartiklar hoppas man förstå fysiken bakom det hela. Filmerna som jag har använt består av flera olika material som har växt fram på ytor av välordnade kristaller i en vakuumkammare. Nanopartiklar har växt fram på självorganiserade halvledare. Dessa system kan ses som prototyper för framtida lagringsmedia. De magnetiska egenskaperna hos

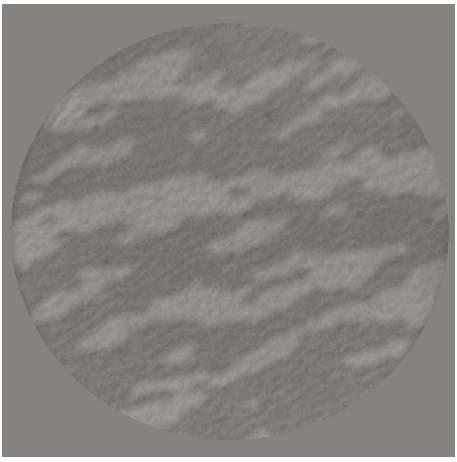

Figure 1.1: Det här är en mikrograf som visar riktningen på de magnetiska domänerna. Dimension på bilden är 10 micrometer och visar att det magnetiska momentet är orienterat i planet.

dessa system är väldigt annorlunda jämfört med magneter som används i vårt dagliga liv. Genom att till exempel manipulera tjockleken av det magnetiska materialet, temperaturen eller tjockleken av ett skyddande lager av något icke magnetisk film ovanpå den magnetiska filmen, kan man ändra de magnetiska egenskaperna i filmen. Metoden som har använts för att kunna studera de magnetiska egenskaperna kallas magnetisk cirkulär röntgen dikroism (engelska benämning X-ray Magnetic Circular Dichroism, XMCD). För att kunna använda denna metod måste man bege sig till en röntgenljus källa med variabel energi, en synkrotron. I Sverige finns en sådan, MAX-lab som ligger i Lund. Den variabla energin gör att man kan undersöka de magnetiska egenskaperna på ett ämne i taget, vilket är viktigt då många prover består av flera olika material. Den totala atomära magneten uppstår alltså som en summa av orbitalbidraget och spinbidraget och finessen med mina mätningar med röntgenstrålning är att vi kan se de olika bidragen separat, vilket är viktigt för att förstå materialens magnetiska egenskaper. Riktningen på det atomära momentet kan bestämmas med hjälp av XMCD. När röntgenljuset infaller parallellt eller antiparallellt med riktning av magnetiseringen hos provet så uppmäter man en signal. Om däremot röntgenljuset infaller vinkelrät med magnetiseringen hos provet försvinner signalen. Genom att använda de tre spektra som man får ut och XMCD reglerna så kan man räkna ut spinnmomentet och orbitalmomentet från varje enskild atom. Det finns ingen annan teknik än XMCD som klarar av detta och det är viktigt för att kunna fastställa den magnetiska anisotropin i provet.

2. Brief introduction to magnetism

2.1 Basic concepts

Magnetism and magnetic phenomena have fascinated people throughout history for over 2500 years. Still, its exploitation and understanding is not yet complete. Historically magnetic phenomena could be studied very early on, by means of the magnetic forces which magnetic materials exert on each other. In more recent times also the forces between magnets and current carrying conductors were studied. Historically, these distinct magnetic forces and interactions could be conveniently described by means of the magnet carrying a macroscopic magnetic moment interacting with the magnetic moments of other magnets or alternatively with the magnetic field created by the other magnetic entities. One possibility to categorize magnetic materials, is to use their response to a magnetic field. The magnetic response of materials in the presence of a magnetic field, can be divided in four distinct categories, and allows to classify them into different types, exhibiting: diamagnetism, paramagnetism, ferrimagnetism, anti-ferromagnetism and ferromagnetism. If we focus on the latter, ferromagnetism, we find the form of magnetism that we are most familiar with in our everyday life, think of refrigerator magnets for example. Among the pure elements in their bulk form, well studied and stable ferromagnets at room or close to room temperature are Fe, Ni, Co and Gd.[1]

At the level of the atom, the existence of an atomic magnetic moment can be related with two facts: the existence of an intrinsic spin magnetic moment of the electron combined with the Pauli exclusion principle. Most elements carry a magnetic moment when isolated as a free atom, but only very few elements exhibit a macroscopic magnetic moment in the condensed phase at room temperature. In an oversimplified picture, for a ferromagnet the myr-

Table 2.1: *The Curie temperature, some magnetic and structural properties for the ferromagnets Fe, Co, Ni.*

Element	Curie T (K)	M_l ($\mu_B/atom$)	M_s ($\mu_B/atom$)	M_l/M_s	Lattice	NN (Å)
Fe	1043	0.085	1.98	0.043	bcc	2.49
Co	1388	0.15	1.62	0.095	hcp	2.51
Ni	627	0.05	0.6	0.083	fcc	2.49

iad of atomic magnetic moments tend to spontaneously align, leading upon vector addition to a macroscopic magnetic moment, susceptible to be used for applications.There is however, also a competition between magnetic order and thermal energy at finite temperatures. As the temperature increases, the thermal energy starts competing with the spontaneous alignment of the atomic magnetic moments. There is a critical temperature, for a ferromagnet known as the Curie temperature, where upon occurrence of a phase transition, the spontaneous magnetization is lost. The macroscopic magnetic order can no longer be maintained at high temperatures. In this work we focus in particular on Co where upon loss of the ferromagnetic order one enters the paramagnetic phase. One should also keep in mind that the Curie temperature is reduced by limiting the size of the magnet drastically down to the atomic regime leading, for example, to ultra thin films and nanometer size ultra thin dots on a non ferromagnetic surface. Within a simple mean field approximation, the Curie temperature is predominantly dependent on the number of nearest neighbors and by drastically limiting the size of the magnet, the average number of nearest neighbor atoms also decreases, leading to finite size effects. The known Curie temperatures for Fe, Co, Ni in the bulk are given in Table 2.1.[2] Finite size effects are often a barrier towards practical applications of ultra thin films or nanomagnet arrays, as they limit the Curie temperature well below room T. As an example, for Co ultrathin films of a few of atomic layers thick, the Curie temperature is only around room temperature.

2.2 Magnetic anisotropy

The magnetic anisotropy energy governs the direction of the spontaneous magnetization in the solid. Phenomenologically, one can distinguish several contributions to the magnetic anisotropy energy: the magnetocrystalline anisotropy which is related to the crystal symmetry of the solid, the shape anisotropy which originates from the long range magnetic dipolar interaction between the magnetic moments, the magnetostrictive or magnetoelastic anisotropy energy dealing with the presence of stress in the solid, and finally the induced magnetic anisotropy, meaning the magnetic anisotropy is induced by means of a thermodynamic treatment, such as heating and cooling under an applied magnetic field. The largest and therefore most important among those energy contributions to the total magnetic energy, are the magnetocrystalline and shape anisotropy. If we go back to the magnetocrystalline anisotropy, the simplest form it takes is a uniaxial anisotropy expressed in a power series of $sin^2\phi$ for bulk cobalt. One can write the magnetocrystalline energy E for an hexagonal lattice, such as for bulk Co, as

$$E = K_0 + K_1 sin^2\theta + K_2 sin^4\theta + (K_3 + K_3' cos(6\phi))sin^6\theta + ... \quad (2.1)$$

where K_0, K_1, K_2... are element specific constants, which temperature dependent. θ is the polar angle between the magnetization vector and the direction of the easy axis and ϕ represents the azimuthal angle. K_1 is generally sufficient to approximate the magnetocrystalline anisotropy energy. The shape anisotropy tends to minimize the magnetic energy by keeping the magnetization within the surface in the case of a thin or an ultrathin magnetic film, therefore it can also be expressed by means of a uniaxial angular dependence, with the easy axis within the surface plane. As the thickness of the material is reduced the surface or interface contributions to K_i become important. Making the thickness, t, dependence explicit one writes

$$K_i = K_i^V + \frac{2K_i^S}{t}. \quad (2.2)$$

K_i^V and K_i^S may have different signs as the environment of the atoms at the interface or surface is strongly anisotropic as compared to the atoms in the bulk.[3],[4] For ultra thin films, a few atomic layers thick, the K_i^S contribution may dominate. Often, but not always, K_i^V favors an in plane orientation. Depending on the sign of K_i^S one can obtain a perpendicular magnetization at low thicknesses. As the thickness increases K_i^V and the dipolar contribution dominate the anisotropy energy and the moment turns in the surface plane: one obtains a Spin Reorientation Transition (SRT). An SRT is observed for both Au/Co/Au and Pt/Co/Pt ultra thin films on various substrates, among the systems discussed in this work. Both these systems, are discussed in literature by means of a K_i^V anisotropy favoring an in plane orientation and K_i^S favoring out of plane.[5]

2.3 Nano-dot arrays: magnetic properties and applications

Magnetic storage has played a key role in audio, video and computer development since its invention. One of the motivations for the research connected with the development of magnetic storage media and high density nano dot arrays is that the preferential direction of magnetization can be changed from in-plane to out-of-plane, facilitating higher storage density. Magnetic nanoparticles commonly consist of magnetic elements such as Fe, Co, Ni, which can be manipulated under the influence of a magnetic field.

Ferromagnetic materials consist of small individual domains in which the magnetic moments of all atoms point in the same direction. This direction

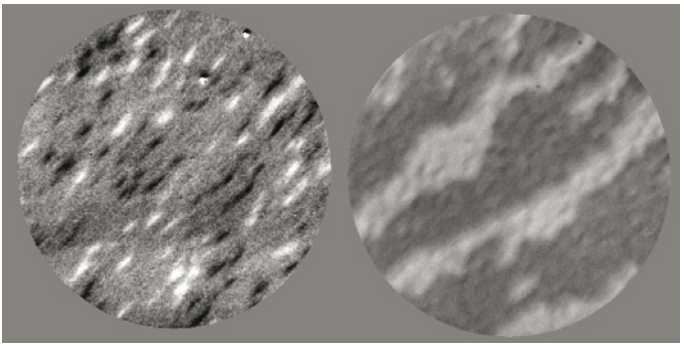

Figure 2.1: XMCD-PEEM micrographs taken at the nano spectroscopy BL at Elettra. *Left panel*: XMCD on 4 ML Co/Pt/SiGe at the L_3 edge (787 eV) Field of View (FOV) 5 μm. The x-rays are incident along the horizontal direction, and at grazing incidence to the surface. Only the in-plane magnetized dots are seen in this geometry. The magnetic contrast difference micrograph shown here, indicate remanently magnetized Co dots at 300 K. We observe both plus and minus orientations in the plane. The dots are elongated perpendicular to the evaporation direction. The gray areas where no XMCD contrast is seen, are most probably out of plane magnetic regions. *Right panel*: XMCD on 3 ML Co/Pt/6 ML Co/Pt/SiGe at the L_3 edge (787 eV) FOV 5 μm. After addition of 2 ML Co, Pt and 3 ML Co only an in plane orientation is observed.

varies from one domain to the next, but what makes ferromagnets useful is the fact that all the domains remain aligned in an external magnetic field even after the field has been switched off. A computer disk, for example, is based on ferromagnetic thin films on which information is stored in submicron sized bits. The magnetic moments within different domains are forced to align with the magnetic field produced by the write disk head. Since the moments in the magnetic domains remain stable, the material remembers whatever information has been recorded. Nanomagnetism basically involves studying how such ferromagnetic materials behave when the magnetic bits or dots are further geometrically restricted, in particular in their lateral dimension. One targets a single domain state for each bit when the bits lateral dimension is well below the micron, one speaks then of a nanomagnet. Nano magnet arrays become particularly interesting when also the thickness of the magnetic material is also reduced. Limiting the thickness of the material to a few atomic layers allows also in some cases such as Au/Co/Au and Pt/Co/Pt, for the magnetization to rotate from in to out of plane due to the magnetocrystalline anisotropy of the surface or interface layers. This effect is known from ultra thin films, but in the case of nano magnets one hopes to obtain directly perpendicularly magnetized individual magnetic bits, which can then be switched by the write head. As the relative strength of the thermal fluctuations increases as compared to the magnetic anisotropy energy of a single dot, as one makes smaller and thinner magnetic dots, one tries to find novel materials with the highest

possible magnetic anisotropy energy, ensuring that the relaxation time, τ, for the magnetization is as high as possible according to

$$\tau = \tau_0 e^{\left(\frac{E}{k_B T}\right)}. \tag{2.3}$$

τ describes the characteristic time during which the magnetization can be considered stable. τ_0 is within the range 10^{-10}-10^{-12} s.[4] E is the magnetic anisotropy energy and needs to be at least of the order of the characteristic thermal energy, k_BT.[6] Under such conditions when the external field is removed the dots will not randomize their direction immediately, but rather it will take some time to do so. This length of time can be anywhere from fractions of a second to years or much longer depending on the value of the dot anisotropy energy, $E = KV$. Larger dots tend to have larger anisotropy energy, due to their large volume. It becomes clear that if we reduce the volume of each dot, we can maximize τ by maximizing the magnetic anisotropy energy. One possibility here in the ultra thin limit, on surfaces, consists of using materials with a magnetocrystalline anisotropy. An alternative may also be to fix the magnetization direction using the exchange bias effect.

2.4 Exchange Bias

The phenomenon known of as, Exchange Bias (EB), was discovered by Meiklejohn and Bean at the General Electric company in 1956, while studying Co particles embedded in their native oxide.[7] It was found that EB occurs when a ferromagnet and a anti-ferromagnet have a common interface. A ferromagnet, such as iron, exhibits a large spin exchange parameter but a relatively small anisotropy energy. This is sufficient to make the ferromagnetic order stable for thicker films, but for ultra thin films or small dots, at finite temperature unstable. In comparison, an AFM exhibits typically a large magnetic anisotropy and consequently very stable magnetic orientations. EB can be thought of arising, in a simple picture, from the exchange coupling between the interface magnetic moments of a FM layer and an AFM layer. The resulting composite magnet exhibits novel properties, with a ferromagnetic response but with a stable magnetization orientation combined with a high anisotropy. A direct result of this effect leads to the hysteresis loop associated with the coupled FM and AFM to be shifted from the zero applied magnetic field value, by a field known as the exchange bias field, H_{EB}. Here, the hysteresis loop shift is determined by

$$H_{EB} = \frac{H_{c1} + H_{c2}}{2} \tag{2.4}$$

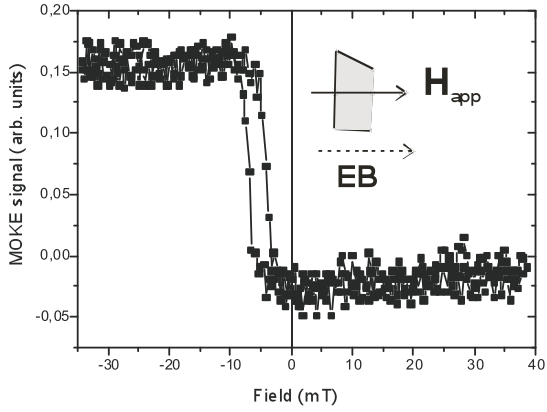

Figure 2.2: Magnetization loop (measured using the magneto-optical Kerr effect) at room temperature (field parallel to the film plane) for a Si(111)/Cu(20 nm)/NiFe(5 nm)/FeMn(10 nm)/Au(1.5 nm) sample. Courtesy of J. Mohanty KU Leuven.

where H_{c1} is the coercive field for the first magnetization reversal after reaching magnetic saturation, H_{c2} is the coercive field for the decreasing positive branch before reaching magnetic saturation.

The most studied samples which exhibit EB, are materials in the form of thin film bilayers. Moreover, bilayers enable the best possible control and characterization of the AFM/FM interface. Often, bilayer systems present also their own limitations in terms of magnetization orientation and possibilities for patterning. One of the alternative ideas for novel magnetic storage media is to exploit self organization on surfaces to obtain dot arrays instead. In the case where one starts with interfaces possessing high magnetic anisotropy energy, or leading to EB, one hopes to gain perpendicular magnetization in a system of magnetically stable and individually addressable nano magnets, within a nano magnet array.

Exchange bias driven anisotropy has long been poorly understood. Following the original idea of Meiklejohn and Bean, a simple approach to the problem, would suggest the exchange interaction between the anti-ferromagnet and the ferromagnet at their interface, as being at the microscopic origin of the exchange bias phenomenon. A soft ferromagnetic film which is exchange-coupled to the anti-ferromagnet will have its interfacial spins pinned given the exchange coupling with the spins of the anti-ferromagnet. Reversal of the ferromagnet's moment will have therefore an added energetic cost corresponding to the energy necessary to create domain walls within the ferromagnet. However, a detailed energy estimate, indicates that not all of the interface spins can contribute to the exchange bias phenomenon. For example, the magnitude of measured the H_{EB} values is typically 100 times less than that predicted, as far as typical numbers of interfacial spins per unit area are concerned, the

exchange constant at the interface, the values of the interface spins as well as the value of the ferromagnet's magnetization. In addition, the exchange bias effect tends to be smaller in epitaxial bilayers than in polycrystalline ones, suggesting an important role for defects. In recent years, progress in the fundamental understanding of the EB effect has been made via synchrotron element-specific magnetic linear dichroism experiments that can image antiferromagnetic domains.[8]

More recently, using the vector character of x-ray magnetic circular dichroism spectroscopy, an XMCD study claimed the existence of interfacial spins that could be linked with the EB phenomenon. This work was performed on the systems NiO/Co, IrMn/Co and $PtMn/Co_{90}Fe_{10}$. Ni and Mn pinned spins were detected at the interface anti-ferromagnet/ferromagnet.[8] The pinned uncompensated interfacial spins constitute only a fraction of a monolayer and indeed do not rotate in an external magnetic field since they are tightly locked to the antiferromagnetic lattice. A simple extension of the Meiklejohn and Bean model can account quantitatively for the exchange bias fields in the three studied systems from the experimentally determined number of pinned moments and their sizes.

2.5 Studying (Ga, Mn)As and MnSb layers: towards novel ferromagnetic semiconductor composite materials

Semiconductor based devices, using electron charge as the information carrier, have been extensively used during the last century and have laid the foundations of the information technology we use today. The gain in performance of these devices has increased by several orders of magnitude over the last decades. The improvements in performance is due to, among other things, the ability in manufacturing and fabrication, which allow to shrink the dimensions of the various logical components and pack them more densely. This ability to increase the component density also leads to faster devices, which simultaneously increase the efficiency and reduce heat loss. However, this route to enhance the performance has come to face difficulties.

The dimensions of the various integrated circuit components, such as transistors, are becoming so small that quantum effects, like tunneling, start to become noticeable and may cause malfunctions. This has been known by the industry for some time, and novel ways to overcome this problem have been introduced to make the devices go even faster. However, all this development will eventually come to an end, at the moment when it is simply not possible to shrink the circuit dimensions further. It is here that spintronic materials enter and may have an impact. For the so called spintronic materials one hopes to exploit not only the charge of the current carriers, but also their spin. This spin functionality may allow to introduce novel electronic components allowing to circumvent limitations introduced by the size reduction. One is therefore look-

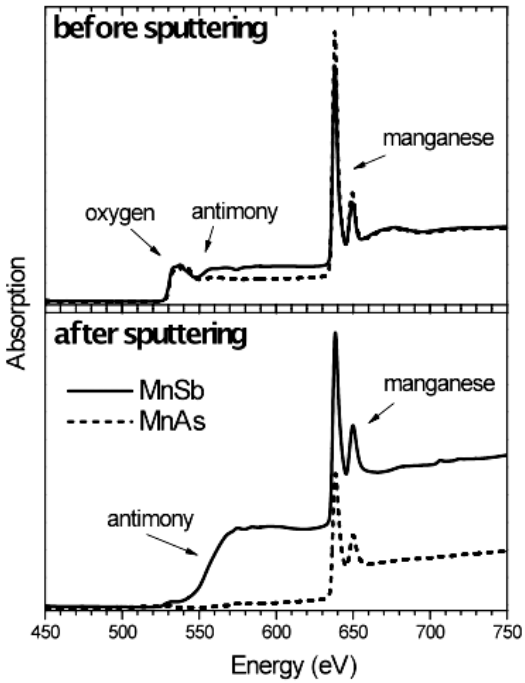

Figure 2.3: X-ray absorption spectra in the total Electron Yield mode are shown. X-ray Absorption allows for an element specific characterization of the near surface region, about 5 nm deep into the sample. The x-ray absorption indicates the existence of oxygen, antimony and manganese edges, before sputtering, for the MnSb sample. The angle of the incident x-rays is 45 degrees to the sample surface. The spectrum for the MnAs sample in the same energy range is shown in comparison, here only manganese and oxygen absorption is observed. After sputtering the sample surface with Ar^+ ions, the oxygen K-edge is not visible any more.

ing for a novel class of materials allowing to combine the use of both electric charge as well as spin upon current flow. One such class of materials, known as Dilute Magnetic Semiconductors (DMS) are considered as good candidate materials for spintronics applications. By doping known semiconductor materials, already exploited in the past by the semiconductor industry, with magnetic impurities, or magnetic clusters, one hopes to give novel functionality to well established materials in the semiconductor industry.[9]

Trying to dope known semiconductor lattices substitutionally with magnetic ions, it turns out that Mn atoms in the few percent range work best among the 3d transition elements, most often the elements leading to ferromagnetism in the solid state, forming only inclusions in the semiconductor lattice. The search for magnetic semiconductors with a Curie temperature, T_c, above room temperature is still a major challenge in semiconductor spintronics. In single-phase samples a T_c = 190K has been reported for (Ga,Mn)As,

a well established material in this research area. Ferromagnetic ordering in these compounds is believed to arise from interactions between Mn local moments that are mediated by holes in the valence band. Hence it is necessary to increase hole concentration in order to achieve higher ferromagnetic ordering temperature T_c, but the equilibrium solubility of Mn in III-V compounds is quite low (about 1 10^{19} per cm^3).[10]

To dope with higher concentration of Mn ions, an effort has been made to grow these compounds by non-equilibrium techniques like low temperature Molecular Beam Epitaxy (MBE). It is of interest, under these conditions, to study the local environment around the Mn atoms. X-ray absorption is an established technique in yielding real space and electronic structure around the photo-excited atom. Here $Ga_{0.94}Mn_{0.06}$As and $Ga_{0.92}Mn_{0.08}$As layers grown on GaAs(100) were studied. The layers were grown at 230 $^{\circ}C$ by means of molecular beam epitaxy in UHV. Some of these samples were subsequently annealed to 500 $^{\circ}C$ and 600 $^{\circ}C$, to induce thermally induced changes in the local structure around the Mn atoms. Studying the x-ray absorption spectra it is found that the local structure around the Mn atoms in the annealed samples, is close to the structure of the hexagonal MnAs reference samples and differs from the local structure of the as grown, non annealed samples. Given the relatively low T_c values achieved so far just diluting ions in a semiconductor lattice hetero-structures consisting of metallic ferromagnetic structures deposited on or buried inside semiconducting materials are considered as an alternative for spintronics applications. One of the potential candidates for integrating ferromagnetic metals with semiconductors and creating magnetic inclusions is MnSb. It has been shown that bulk MnSb has a T_c of 587 K and a room temperature saturation magnetization of 710 emu per cm^3. The $Mn_{1-x}Sb_x$ layers grown on the GaAs substrate are reported to reach a T_c of 620 K.[11] MnSb appears to be a good candidate compound for forming nano-inclusions that are ferromagnetic above room temperature within semiconductor lattices.

Fig. 2.3 shows x-ray absorption spectra taken in the so called electron yield mode. Here, as will be discussed more in detail later the secondary electrons are collected after soft x-ray excitation. The various elements are visible given the sudden increase of the absorption coefficient as the photon energy is varied, at the corresponding edges. The oxygen K-edge (around 530 eV) and Mn L_3 and L_2-edges (features around 638 and 649 eV) as well as the Sb $M_{5,4}$ edges also in the photon energies above 500 eV. One can identify the elemental composition of the sample under study as it is treated *in situ*. Upon sputtering with Ar ions the oxygen impurities on the MnSb sample surface are removed. Here MnSb is studied given the fact that it is a well studied ferromagnet containing Mn susceptible to lead to magnetic inclusions in other semiconductors. MnAs is studied here only as a reference sample. As a first step here MnSb layers are studied grown on GaAs(100) and GaAs(111) substrates. The observed diffusion of Ga atoms from the substrate to the layers results in the formation of an additional Mn-rich cubic phase of GaMnSb. In

the case of the (100) oriented substrate, the diffusion of Mn into the substrate is additionally found.[12] Here soft x-ray absorption spectroscopy allows for an element specific characteristic of the near surface region of this compound. A Mn-rich near surface region is found. The investigations of chemical bonding and local atomic structure around Mn atoms by x-ray absorption indicate the presence of high structural and chemical disorders in both layers, which result in the lowering of the spin magnetic moment in remanence located on the Mn ions of 1.3 μ_B and the increase in the orbital moment moment of up to 0.17 μ_B per Mn atom in remanence. This is a strongly enhanced value for the orbital moment and would correspond to a value of about 0.45 μ_B per Mn atom under magnetic saturation conditions.[13] An enhanced orbital moment and a reduced spin moment, is most likely caused by the presence of different phases and a Mn-rich surface in the investigated samples. The fact that the MBE grown MnSb compound on GaAs substrates exhibit the natural tendency to form inclusions indicates the compound to be a good candidate to form nano-inclusions embedded inside the semiconductor.

3. Synchrotron Radiation based Techniques

3.1 Synchrotron Radiation

Synchrotron radiation is electromagnetic radiation which is emitted from charged particles when they undergo acceleration (or deceleration). Electrons or positrons are typically used due to their low mass. At MAX-lab, the light source we mostly discuss here, electrons are stored in the storage ring of MAX II. These circulate at speeds very close to the speed of light, under relativistic conditions, for example at MAX-lab the energy of the stored electrons is 1.5 GeV. This concept is used generally at synchrotron facilities, the electrons being kept in the storage ring, in a stable orbit, in packets or bunches, emitting radiation, for example, upon deflection, or controlled undulation, by means of a magnetic field. The demands to the storage ring components both vacuum wise and magnet lattice wise are very high to be able to keep the electrons circulating in a stable orbit. There has to be Ultra High Vacuum (UHV) in the storage ring to keep the electrons from colliding with rest gas atoms and molecules. This is achieved by using a large range of different pumps. At low speeds the electrons emit radiation with an angular distribution of $\sin^2\theta$, where θ corresponds to the angle between the acceleration and observation directions. However, for particles traveling at relativistic speeds, there is a dramatic effect for an observer in the rest frame of the laboratory. This observer will perceive the radiation distribution as an extremely forward pointing cone of radiation. This makes synchrotron radiation sources, specially the most modern ones like MAX II, one of the brightest sources of x-ray light on earth. The observed frequency spectrum of the synchrotron radiation is very wide, extending from the visible range to the hard x-ray radiation, and will be shifted to high energies because of the

Table 3.1: *MAXII storage ring specifications at MAX-lab. The straight sections can be used for insertion devices.*

Circumference (m)	90
Injection energy (MeV)	400
Operating energy (MeV)	1500
Maximum stored current (mA)	280
Nr of straight sections	10

relativistic speed of the electrons that changes the observed frequency due to the Doppler effect. The advantages of using synchrotron sources lead to the continuously increasing number of users, since the 1970's, where the first machines started delivering radiation on a routine basis. More recently magnet devices were built which enhance the intensity and influence the energies of the emitted radiation emitted and were built into the existing storage rings. Nowadays, fourth generation sources are being built, that will include different concepts to produce even brighter x-ray sources.

3.1.1 Soft x-rays: BL D1011 at MAX-lab

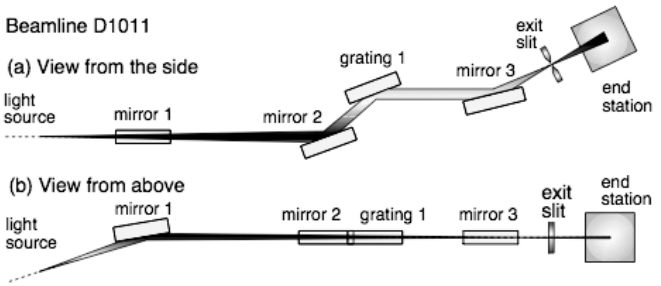

Figure 3.1: Schematic optics layout of beamline D1011 at MAX-lab. This grazing angle optical setup ensures that the photon beam focus is found at the exit slit for energies between 30-1500 eV. The end station shown here, is the front chamber at about 15 m from the source. When the front chamber is not used, the x-ray beam propagates through the front chamber and is refocused into the back chamber (not shown here) used for magnetism experiments.

Beamline D1011 is a soft x-ray beamline at MAX-lab. Beamline D1011 is based on a bending magnet x-ray source, the beamline covering the energy range 30 to 1500 eV, with a high photon flux, $10^{10} - 10^{11}$ ph/s for linearly polarized x-rays.[14] The difference with this beamline compared to other beamline's at MAX-lab is the adjustable local bump of the electron beam trajectory providing out of plane radiation making it suitable also for XMCD measurements. As explained in detail later, when out of plane bending magnet radiation is collected, the state of polarization is elliptical or even close to circular. There are two experimental stations attached to the beamline, the front chamber and the back chamber given their location at the beamline, both of which are Ultra High Vacuum (UHV) measuring stations. The front chamber consist of a preparation chamber and an analysis chamber located below the preparation chamber, separated with a manual valve. A manipulator is placed on a precision X-Y table on top of the preparation chamber, enabling transfer of the sample between the two chambers and also movement in the

XY-plane. Nowadays, the front chamber is rarely used for magnetic measurements due to the photoemission setup there, which does not allow the user to apply magnetic fields *in situ* at the measuring position. Instead the second experimental station is used, a chamber specifically designed for XMCD measurements. This back chamber which is specially designed for magnetic measurements has a special geometry including rotatable UHV coils, a setup shown in Fig. 3.2 which the front chamber lacks. These coils possess a cooling system which allow measurements under applied magnetic field, essential for magnetizing the sample and in particular measuring element specific hysteresis loops. The manipulator rod of the back chamber provides the possibility to cool the sample down to 20 K with liquid helium or 100 K with liquid nitrogen. Compared to the front chamber the back chamber offers the possibility to add more sample preparation equipment due to the higher available number of flanges.

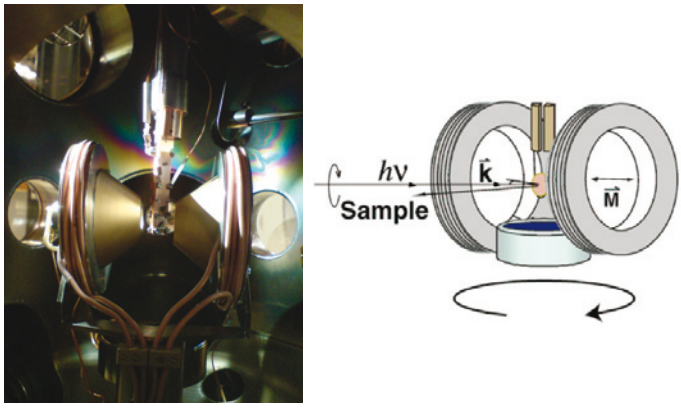

Figure 3.2: Left panel: Experimental geometry of the back chamber at D1011, MAX-lab. The x-rays enter the chamber from the upper left. The XMCD intensity is proportional to, $\mathbf{k} \cdot \mathbf{M}$, $\mathbf{k}$ the x-ray wavevector, $\mathbf{M}$ the sample magnetization direction. With two independent polar rotation axis, both the easy and hard magnetic direction can be probed for XMCD. The polar rotation of the coil pair is controlled from below. Polar rotation of the sample is independent and controlled from above. Using soft iron cores, yields a magnetic field up to 800 Gauss at the sample. *Right panel*: Here the same setup is shown schematically. For clarity it is shown without the iron cores. Now the channel plate detector positioned below the sample, can be clearly seen.

3.1.2 Future outlook: the new beamline I1011 at MAX-lab.

In the present work use was made of circular soft x-ray light produced by the D1011 bending magnet x-ray source at the MAX II storage ring. The multi purpose beamline D1011 of MAX-lab is based on dipole magnet radiation. To obtain circular x-rays a local bump is produced in the electron orbit. One

views the electron beam from a small out of plane angle. An out of plane local bump is a very cost effective way to obtain circular x-rays. The fact that one has locally an out of plane source increases the chances of rather strong intensity fluctuations. When a high degree of circular polarization is used there is a strong decrease of photon flux, in particular above 1 keV. An alternative solution to obtain x-rays of variable polarization is to obtain a more complicated magnet structure in the storage ring to act as the x-ray source such as an Elliptically Polarizing Undulator (EPU). In the case of an EPU one can in principle obtain circular x-rays of both high photon flux and brilliance.

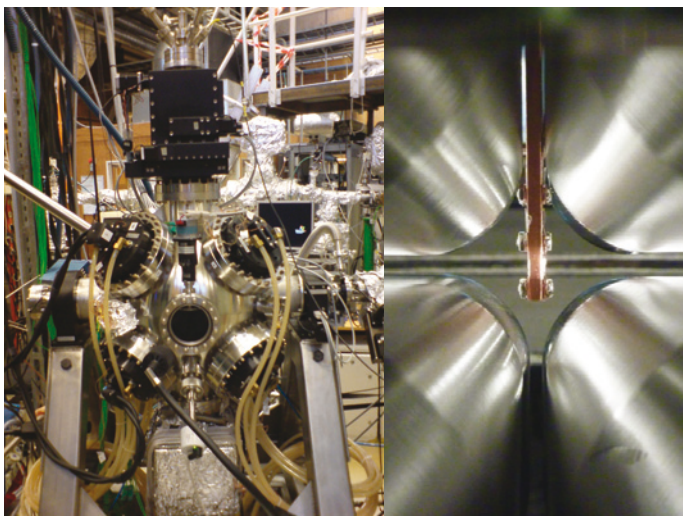

Figure 3.3: Left panel: The octupole end station is shown. One can see four of the magnetic poles, the inlet and outlet of the cooling coil medium can be distinguished. *Right panel*: A picture of the inner part of the octupole. The sample holder and sample rod is seen in the vertical direction. The UHV stainless steel cans housing the coils are clearly seen.

The I1011 beamline at MAX-lab, located at the MAX II storage ring, uses an EPU light source, which produces soft x-rays of a variable polarization state. The I1011 beamline is based on a collimated Plane Grating Monochromator (cPGM) provided by the BESTEC company (Berlin, Germany). The cPGM covers high photon flux and good energy resolution in the energy range of 0.1-1.7 keV using three *in situ* exchangeable plane gratings. Compared to D1011, this beamline delivers a larger photon flux, as well as brightness and gives full control of the degree of x-ray polarization over the whole energy range covering the absorption edges of all relevant elements, for magnetic measurements. Furthermore, one important upgrade with this beamline compared to D1011, is that the end station is planned to be frequently exchanged. Changing the end station gives the experimentalist more ways to gather information about the magnetic materials in question. There will be three end

stations to switch between. At D1011 only an Ultra High Vacuum (UHV) end station allows for the application of moderate magnetic fields, of up to 800 Gauss in the horizontal plane. At I1011 in comparison, an octupole magnet end station, and a superconducting magnet end station allow for the application of higher magnetic fields.

The UHV octupole magnet end station has been specially engineered to solve problems which arise for magnetic measurements see Fig. 3.3. This UHV end station contains eight water cooled electromagnets, spaced equidistantly over the surface of a sphere. This allows for the application of the field in any direction. The whole chamber rotates around the beam axis, which allows for measuring the magnetic properties with a variable geometry of applied magnetic field, electromagnetic radiation and sample orientation. These high current magnets generate a vector magnetic field in the sample space of up to 1 T. Here a different concept than at the multipurpose station at beamline D1011 is followed. One limits the available space of the sample. Stainless steel cans are used, to house the electromagnetic coils, which withstand a pressure difference of about 5 atmospheres. These cans approach the sample within a couple of cm. Water under pressure, shielded from the UHV by the stainless steel cans cools the coils. A compromise needs to be made in field strength given the size of the sample and of the sample holder. A free space of a 2 cm radius is left free along the three main axis which are perpendicular to the faces of a cube. The coils axis are pointing along the cube diagonals Fig. 3.3. Such an end station has obvious advantages for the magnetism related applications but severely limits the possibilities for UHV *in situ* sample preparation. In terms of sample preparation, the sample needs to be treated in a separate part of the chamber, for sputtering or evaporation using a sample transfer sample holder. Still, many more possible experimental geometries for resonant reflectivity and absorption measurements can be realized. For example, for the case of systems exhibiting exchange bias, as discussed within this thesis frozen spins can be identified comparing pairs of spectra taken in a chiral configuration. With the octupole end station it is much easier to modify the scattering geometry required given the vector character of the magnetic field.

3.2 X-ray Absorption Spectroscopy (XAS)

X-ray Absorption Spectroscopy (XAS) is an experimental technique that yields information on the local electronic structure of the sample, around the photo-excited atom, yielding also, magnetic and structural information. This information can be extracted once measurements are made using several polarization states of the x-rays, as well as working at both the near edge regime and at higher photon energies. XAS is based on the selective excitation of core electrons to unoccupied electronic states by means of photons, according to the dipole selection rules. The incident photon must

have an energy equal or larger than the difference in energy between the initial state and the unoccupied final electronic state, for the x-rays to be absorbed. Indirectly this creates a problem, in particular for the soft x-rays used here, thick samples can not be measured in a transmission geometry for their x-ray absorption, due to the penetration of the soft x-rays in a metallic sample, about 0.1 micron for typical metals. Only ultra thin samples can be investigated this way with a thickness of much less than the penetration depth of the photons. Here one exploits that in the excited state the system is not stable and thus releases its extra energy after a short time. There are in principle two ways for this happen; by emitting a fluorescence photon or by emitting an Auger electron, see Fig. 3.4. The process by which the electron is emitted is known, in the soft x-ray domain, as the Auger decay process see Fig. 3.4 and it is this process which statistically dominates here the filling of the core hole, after excitation and on which we rely upon to perform our measurements. To monitor the number of Auger electrons we use a Multi Channel Plate (MCP) detector and also simultaneously measure the electric photo-current or the sample drain current that the Auger process induces on the sample. It can be shown that for the samples investigated here both these signal channels are proportional to the absorption coefficient μ. During this work the MCP detector hasn't been working as efficiently as the drain channel, due to a higher lever of noise. One needs to repeat a measurement several times given the small XAS signals produced by samples often in the submonolayer range on surfaces. The typical escape length, λ, for the electron contributing to the drain or MCP signal is of order 2 nm for the late 3d elements. One probes with the drain signal mostly the near surface region of the sample. The photon penetration and escape length are much larger, of order of several 10 nm.

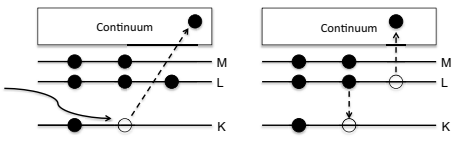

Figure 3.4: Here is shown a schematic picture describing the x-ray absorption (left) and the Auger electron emission process (right), in terms of single electron states.

3.2.1 Depth probing in electron yield

The incident radiation, here x-ray photons, is sufficiently energetic so that it penetrates deeply into the solid, well beyond the escape depth for the characteristic secondary electrons, λ. The electron escape depth is limited by the electron mean free path, which is the average distance traveled by an electron in between elastic or inelastic collisions. The mean free path depends on the kinetic energy of the electron and can be described by the so called universal

curve for many solid materials. At low kinetic energy the electrons have a long mean free path and should in principle be able to escape the sample, but since they have very low kinetic energy the electrons will not be able to overcome the work function. Therefore, the electron escape depth is relative short, about 17 Å for the L-edges of the late 3d metals. Due to the finite electron escape depth of the secondary electron, the total electron yield mode mainly probe the near surface region.[15] The energy dependent total electron yield mode Y(E) for normal incidence can be expressed as

$$Y(E) \propto \int_0^\infty I(x,E)\mu(E)e^{-\frac{x}{\lambda}}dx \tag{3.1}$$

where x is the depth away from the surface, where the absorption process takes place, $\mu(E)$ the photon absorption coefficient and λ the electron escape depth. $I(x,E)$ represent the intensity of the x-rays, at a certain photon energy E at the depth x and is expressed as

$$I(x,E) = I_0(E)e^{-x\mu(E)} \tag{3.2}$$

where $I_0(E)$ is the incident x-ray intensity. However, although the incident photons penetrate several hundred Ångströms deep into the sample for soft x-rays, the number of electrons that can escape from the surface decreases exponentially with the thickness, x away from the surface.

The physical origin of a finite electron escape depth is the inelastic scattering of the electrons. Successive inelastic scattering results in an electron cascade, where multiple low energy electrons are produced from a high energy electron. Eventually, when the multiple low energy electrons have a kinetic energy lower that the work function of the sample material, the cascade electrons cannot escape from the sample surface, leading to a finite electron escape depth.

3.2.2 X-ray magnetic circular dichroism (XMCD)

X-ray magnetic circular dichroism (XMCD) is an experimental technique that enables quantitive determination of the magnitude, direction of the spin and orbital moments in an element specific way.[16] Important about this technique is its sensitivity to study very dilute samples. This enables studies of ultra thin magnetic films and two dimensional arrays of magnetic nano structured samples. The XMCD technique relies on spin selective photon excitation from the spin orbit split core electronic levels. One uses circularly polarized x-ray light to transfer the photon angular momentum $\hbar$ to the sample along the magnetization direction. This leads to the vector magnetometry character of the XMCD technique, the dichroic intensity being proportional to $\mathbf{k} \cdot \mathbf{M}$. The dipole selection rules, using circular light, allow for transitions from the

$2p_{3/2,1/2}$ initial states to the empty 3d levels, with spin selectivity. The unbalance of the empty 3d final states caused by the exchange splitting of the 3d final state leads to a spin selective absorption process and yields information about the spin polarization of the 3d states. The spin moment (m_s) is simply given by the difference between the number of spin up (N+) and spin down (N-) 3d holes, reflected in the intensity of the $2p_{3/2,1/2}$ white lines.[17] Here we illustrate XMCD by data on a permalloy film capped with 1.5 nm Au layer.

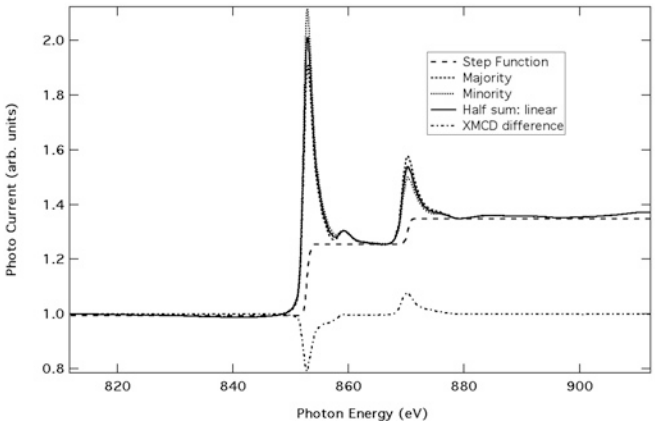

Figure 3.5: XAS spectra of Ni in a permalloy thin film (80 % Ni, 20 % Fe) at BL D1011, with an x-ray angle of incidence of 45°. Clear dichroic effects are seen in the L_3 and L_2 white lines as the magnetization is reversed. The XMCD difference spectrum is obtained by subtracting the XAS minority spectra from the XAS majority spectra. Here the difference spectrum is shown after addition of 1 to obtain all curves in the same scale. Using the magneto optical sum rules and introducing the double step function, the orbital (m_l) and the spin (m_s) moment can be determined directly in μ_B per Ni atom with elemental specificity.

3.2.3 XMCD Sum Rules

Determining the atomic spin- (m_s) and orbital- (m_l) magnetic moments from XMCD data one can use the XMCD sum rules, where ΔL_3 and ΔL_2 are the areas of the L_3 and L_2 white line asymmetries (dash-dotted line Fig. 3.5).[18][19]

$$\Delta L_3 + \Delta L_2 = -\frac{C}{2\mu_B} m_l \tag{3.3}$$

and

$$\Delta L_3 - 2\Delta L_2 = -\frac{C}{3\mu_B}(m_s - 7m_T) = -\frac{C}{3\mu_B}(m_s^{eff}) \tag{3.4}$$

The constant C is governed by the degree of circular polarization of the x-rays and the number of empty 3d states (n_d).[20] The latter can be determined to a very good approximation for the systems studied here using the halfsum of the minority and majority spectra. The number of empty 3d states can be obtained from theory or an experimental standard. There is a simple rule one can use as a starting point in the analysis for the number of 3d holes regarding the stable ferromagnets at room temperature Fe, Ni and Co. Following theoretical estimate Cu atom can be attributed a 3d hole count of 0.8 in the bulk, and then by moving backwards in the periodic table to Ni one adds 1, giving the number of empty 3d states for Ni to be 1.8, 2.8 for Co and finally 3.8 for Fe.[21] These numbers, valid for the bulk, vary of course given the atoms local environment, however they constitute a good starting point for these atoms in the metallic state. The use of an experimental standard allows an independent experimental determination of this number. Furthermore,

$$m_T = \langle T_Z \rangle \frac{\mu_B}{\hbar} \tag{3.5}$$

where m_T is the appropriate component of the d electron expectation value of the intra-atomic magnetic dipole operator.[18] $\langle T_Z \rangle$ is the expectation value of the magnetic dipole operator. It is due to an anisotropy in the spin moment and can be induced by an anisotropic charge distribution around the atom. This is a corrective term, which for single crystalline systems, can be determined by angle dependent measurements.[22]

3.2.4 Applicability and Validity of the XMCD Sum Rules

There has been a lot of debate, which is still ongoing, about the theoretical validity as well as the experimental applicability of the XMCD sum rules. According to Thole et al. the error made in the approximation used to derive the orbital sum rule, the difference in the radial parts for the transition matrix elements for both edges is neglected. This is of the order of 1 % for the $L_{2,3}$ edges of 3d transition metals.[19] Moreover, band structure calculations estimate on some model systems a maximum error in the value of m_l of about 10 %.[23] Regarding the spin sum rule it is necessary that the L_3 and L_2 edges are fully separated from each other. This is not possible unless the 2p spin orbit coupling is much larger than the Coulomb interactions in the final state. For the 3d transition metals this error is relatively small, estimated to less than about 5 % for Ni.[18] Another problem is the presence of the charge distribution around the atom, which can be anisotropic, as is usually the case at surfaces and interfaces. The anisotropy of the charge distribution can be determined by means of angular dependent measurements, depending on the symmetry of the sample in question.[24] Also, to apply the XMCD sum rules, an accurate knowledge of the number of 3d holes is needed. This can be acquired by typically measuring a reference sample, also known as a standard, containing the

same element in question, in a rather close chemical state if possible, where the orbital and spin moments are known, to obtain the number of d holes. An experimental problem that arrises and needs to be taken into account for an accurate determination of 3d holes is magnetic saturation, source coherence effects and saturation effects in the secondary channel.[25]

3.2.5 Polarimetry by means of XMCD

X-ray polarimetry measurements and their analysis leads to the characterization of the polarization state of the synchrotron light at a specific energy range. The polarization state of the x-ray light used plays an important role in how the, typically elliptically polarized, synchrotron radiation x-ray light interacts with matter. In particular, the application of the XMCD technique, once the polarization state of the x-ray light is known, leads to the value of the spin and orbital moments. A precise determination of these magnetic moments requires a well defined degree of circular polarization, P_c, in order to obtain a correct value of the atomic spin moment using the XMCD sum rules, Fig. 3.6 shows P_c for D1011. Using a bending magnet as the x-ray source, the radiation observed in the plane of motion of the electrons, also the plane of the storage ring, is linearly polarized. The further out from the storage ring plane one observes the bending magnet radiation the more the light is circular. Enough circular light is obtained for a small out of plane angle as the emitted radiation from the electrons is contained in a narrow cone due to the relativistic nature of the orbiting electrons in the storage ring.

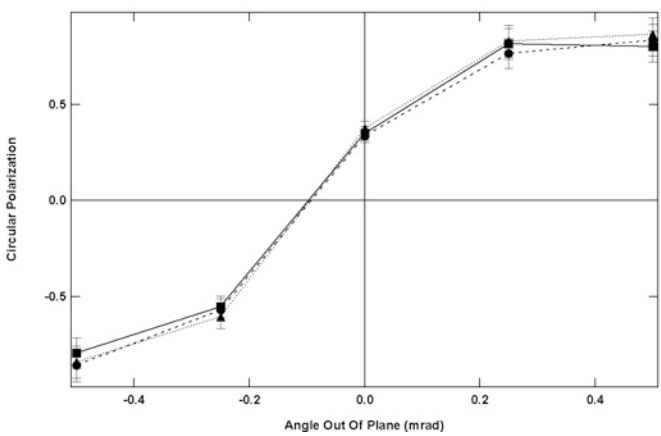

Figure 3.6: The curves give the degree of circular polarization, P_c, as the x-ray source is moved in the vertical direction relative to the monochromator. These data, taken during 2004 and 2005, illustrate that at the particular time of these measurements the off plane angle of the local bump needed readjustments.

A consequence is then going out of the storage ring plane, that the higher degree of circular polarization will come at the expense of the photon flux. Using the in plane and out of plane components of the electric field of the radiation the degree of circular polarization can be expressed as,[26]

$$P_c = \frac{2E_\perp E_\parallel sin^2(\Delta\phi)}{E_\perp^2 + E_\parallel^2} \tag{3.6}$$

were $\Delta\phi$ is the phase shift between the horizontal $(E_\parallel)$ and vertical $(E_\perp)$ E-fields. Assuming that $\Delta\phi = \pi/2$, $I_\parallel = E_\parallel^2$ and $I_\perp = E_\perp^2$ the equation reduces to the more familiar form,

$$P_c = \frac{2\sqrt{I_\perp I_\parallel}}{I_\perp + I\|} \tag{3.7}$$

and the degree of circular polarization can ideally be determined once the two orthogonal electric field components are determined.

To make such a determination on a routine basis, a well known magnetic standard can be used. An easy way to determine the degree of circular polarization is to calculate the atomic orbital and spin moments of the standard, which are known. The standard sample is usually a thick film of Co, Ni or Fe where the atomic spin and orbital moment is previously determined by means of conventional magnetometry and if possible already by means of XMCD as well. The five fixed positions at BL D1011 at MAX-lab in the radiation cone are defined here as:

- π light, σ +1/2, σ +1, σ -1 and σ -1/2.
- π light corresponds, for the D1011 beamline of MAX-lab, for a fully in plane x-ray observer, to linearly polarized light with the polarization plane in the plane of the motion of the electrons, $P_c = 0$.
- σ +1/2 to out of plane angle of 0.25 mrad "above". Elliptical light with $P_c = +0.64$
- σ -1/2 to out of plane angle of 0.25 mrad "below". Elliptical light with $P_c = -0.64$
- σ +1 to out of plane angle of 0.5 mrad "above". Elliptical light with $P_c = +0.93$
- σ -1 to out of plane angle of 0.5 mrad "below". Elliptical light with $P_c = -0.93$

The acceptance angle of the SX700 Zeiss monochromator of the D1011 beamline is 0.2 mrad. Choosing one of these positions and an already determined standard sample, the degree of circular polarization, P_c, is easily determined knowing the spin and orbital moments of the standard. This is not of course a complete determination of the electric field components, it only

serves the purposes of magnetic moment determination in ferromagnetic samples, where linear dichroism effects can be neglected.

A complete determination of the polarization state of the x-ray light would require the direct determination of the in plane component of the electric field as well as possible contributions of un-polarized radiation.

3.3 Nanospectroscopy at Elettra: XMCD-PEEM

Photo-Emission Electron Microscopy (PEEM) combines the photoeffect with electron microscopy, using the radiation of monochromatic x-rays onto the sample surface, which leads to emission of electrons. Imaging and microscopy is possible in the case of the photo- or Auger-electrons using lenses based on electric or/and magnetic forces. Here the electrons are produced much like in the XAS process after a 2p core level excitation. As only the electrons from the first layers are predominantly emitted, PEEM is a surface technique . The excited electrons are accelerated towards the microscope, an electrostatic objective lens and a projective lens will then magnify and image the electron yield on a two dimensional electron detector. The visible light image emitted from the detector can then be recorded using a CCD camera. It is a common feature of all cathode lens microscopes that the sample itself, as the cathode, is part of the optical system. The outer electrodes are on the same potential as the microscope housing, while the inner electrode is at a high negative voltage. The equipotential lines produced by such a arrangement resemble the shape of a thick concave optical lens.[27]

Beamline

source:	2 Apple II type undulators 10 cm period, with phase modulation electromagnet
flux:	2 x 10^{13} photons/sec @ 150 eV 200mA ring current, 2.0 GeV; 10 µm exit slit opening
range:	50-1000 eV
resolving power:	4000 @ 400 eV
polarisation:	linear horizontal, linear vertical, elliptical
angle of incidence:	16° sample-photon beam

SPELEEM microscope (first branch)

Lateral resolution	
XPEEM imaging:	40 nm routinely
XMCD-PEEM:	50 nm
LEEM:	15 nm
energetic resolution	
spectral imaging:	300 meV
micro-XPS:	200 meV
field of view (min-max)	
X-PEEM mode:	2.5µm - 10µm
LEEM mode:	2.5µm - 50µm
microspot size:	20 µm× [2-5]µm (hor. x vert.) on the sample

Figure 3.7: PEEM specifications at Elettra for the 1.2L Nanospectroscopy beamline. This is one of the beamlines and instruments, probably offering the highest lateral resolution within the EU.

3.4 Hard x-rays at MAX-lab I811 and HASYLAB A1

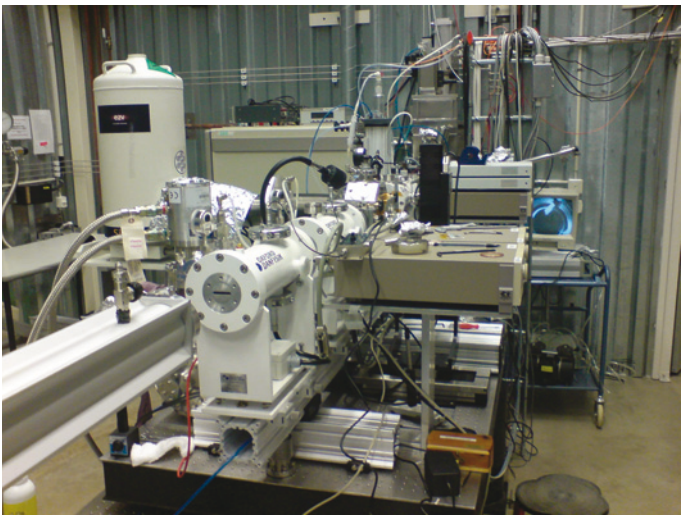

Figure 3.8: The experimental area at I811 at MAX-lab. This is a beamline dedicated to X-ray Absorption Finestructure Spectroscopy (XAFS) and X-ray Diffraction (XRD) experiments with an energy range of 2.3-20 keV. At the left side the LN_2 tank of the multi-element fluorescence detector is seen. The sample is located within a chamber filled with He gas, to reduce x-ray losses and assure an inert chemical environment for the sample. In the front part of the picture one sees one of the ionization chambers (Oxford-Danfysik) used for XAS in transmission x-ray mode.

Beamline I811 at MAX-lab is based on a superconducting multipole wiggler, dedicated for X-ray Absorption Finestructure Spectroscopy (XAFS) and X-ray Diffraction (XRD) experiments. The energy range is from 2.3-20 keV and the beam size on the sample is 1 mm in diameter.[28] The optical layout is common to many other synchrotron facilities with wiggler, collimating mirror, double crystal monochromator, focusing mirror and then experimental station. The energy range is reached by using interchangeable pairs of Si(111) and Si(311) crystals. The first crystal is mounted on a bender mechanism and the large heat load from the x-rays is removed by the water cooling and the remaining distortion of the crystal shape is corrected by a bending mechanism. The second crystal provides a variable focusing by a cylindrical bending, variable curvature radius. Each crystal has a piezo drive for fine adjustments. The second crystal piezo drive is used for automatic detuning and monochromator stabilization. Beamline A1 at HASYLAB is similar in optical layout to I811 at MAX-lab. The biggest difference is the energy range, the covered energy range was (2.4) 5 - 18.5 keV using the Si(111) crystals and (6) 10 - 32 keV using the Si(311) crystals.[29] The standard sample holder allows measurements at room temperature and at liquid nitrogen temperature, optional equipment can be mounted for additional cooling with liquid He.

3.4.1 Fluorescence detection

The fluorescence technique for recording x-ray absorption spectra is especially useful for investigations when surface information from electron yield is not enough. This is the technique of choice in particular for hard x-rays at I811 or HASYLAB. In the fluorescence detection cases, the signal is directly proportional to the absorption coefficient in question. However, the fluorescence yield is low, and the secondary radiation is much weaker than the primary beam. Because of this very efficient, multi-element fluorescence yield detectors are used. The presence of several crystals allows to circumvent in the EXAFS mode, Bragg peaks originating in the substrate, in the case of ultra-thin adsorbate films studied here.

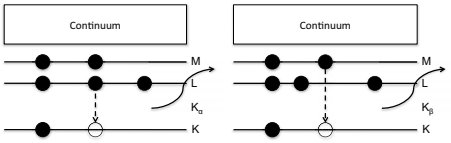

Figure 3.9: A schematic picture is shown here, describing fluorescence x-ray emission in terms of single electron states. Two different processes for the filling of the core hole are schematically illustrated.

3.5 Extended X-ray Absorption Fine Structure (EXAFS) basics

Extended X-ray Absorption Fine Structure (EXAFS) refers to the modulation of the absorption coefficient seen typically in the energy range 40-1000 eV beyond a core level absorption edge. The intensity modulation seen at lower photon energies close to the edge is often referred to as X-ray Absorption Near Edge Spectra (XANES). EXAFS is a final state interference effect, where the interference develops as the propagating photoelectron in the material interferes with contributions from scattered electron waves from neighboring atoms. At high kinetic energies for the outgoing photoelectron wave backscattering dominates. This interference between the outgoing wave and incoming wave will give rise to the oscillatory variation of the absorption coefficient, μ, in the EXAFS spectra beyond the absorption edge, Fig. 3.10.[30] This is described by the characteristic EXAFS function $\chi(E)$

$$\chi(E) = \frac{\mu(E) - \mu_0(E)}{\mu_0(E)} \tag{3.8}$$

where $\mu(E)$ is the measured absorption and $\mu_0(E)$ is the atomic background absorption. To obtain access to physical parameters from the EXAFS, it is

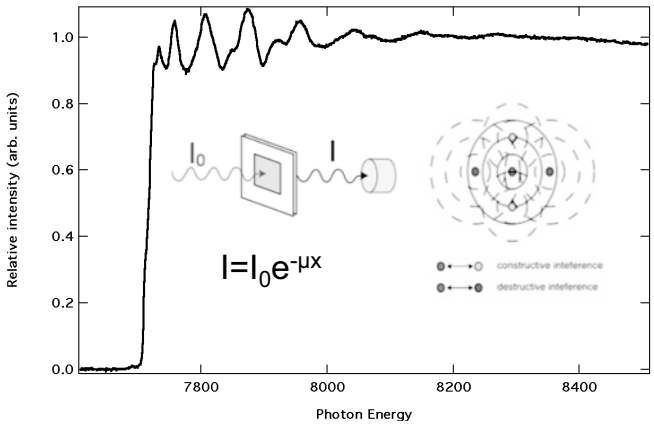

Figure 3.10: The x-ray absorption for a Co foil at the K-edge. EXAFS oscillation are seen extending several 100 eV above the K-edge. *Left inset*: The experimental geometry to take these data is shown as an inset. Here the most straightforward way to determine absorption coefficient μ, is to measure the intensity of the transmitted light I and then apply the Beer-Lamber law to determine μ for different energies. Alternatively μ is proportional to the amount of electrons emitted in the secondary electron Auger process, or fluorescence process. *Right inset*: The underlying physics of the EXAFS process is illustrated. The photoexcited electron is scattered by the neighbor atoms yielding constructive and destructive interference of the electron wave, leading to the EXAFS.

necessary to convert the photon energy E into the photoelectron wavevector k, in order to relate $\chi(E)$ to structural parameters, using,

$$k = \sqrt{\frac{2m}{\hbar^2}(E - E_0)} \tag{3.9}$$

Here k is the wave vector of the photoelectron, assuming a quasi free photoelectron in the final state, propagating inside the solid, for high photoelectron kinetic energies. E_0 is the energy at the inflection point at the absorption edge. All this yields to the transformation of $\chi(E)$ in E space to $\chi(k)$ in k space where,

$$\chi(k) = \sum_j N_j^* S(k) F_j(k) e^{-2\sigma_j^2 k^2} e^{\frac{-2r_j}{\lambda_j(k)}} \frac{sin(2kr_j + \phi_j(k))}{kr_j^2} \tag{3.10}$$

N_j^* is proportional to the number neighboring atoms of the j^{th} type with the backscattering amplitude $F_j(k)$ for each scattering path, with a Debye-Waller factor of σ_j accounting for thermal vibration and static disorder. N_j^* contain also the information on the angular dependence of the angle between the bond

of atom j with the central atom i and the electric field. $\phi_j(k)$ is the total phase shift experienced by the photoelectron due to the Coulomb potential of the central atom and the backscattering. The term $e^{-2r_j/\lambda_j(k)}$ arises from inelastic losses due to neighboring atoms in the scattering process with λ_j being the electron mean free path. $S(k)$ is the amplitude reduction factor due to losses in the electron propagation process. Equation 3.10 used here is only valid within the so called Gaussian or harmonic approximation, as only a Gaussian pair distribution function is considered.[31][32]

4. Sample Preparation

4.1 Reference sample

As described earlier a standard, or reference, sample is needed for one to be able to determine the spin- and orbital moments as accurately as possible. In our case, the reference sample is usually prepared using one among three possible different ways. First, a thick sample, prepared earlier *ex situ*, is put into the chamber together with the actual unknown samples which are going to be measured. Typically such a standard is prepared on the same substrate material, the substrate being flat, in contrast with the nano structured surface used for the unknown sample. Second, the reference sample is made during the measuring time, *in situ*, like for the previous preparation. Finally, one of the actual samples have been prepared with the magnetic element with high thickness so that it can also be used as a reference sample, as it approaches bulk like properties. These three types of standard samples mentioned here, have been used at different times, depending on what type of samples have been measured.

4.2 Shadow evaporation on nano-structured surfaces

Depositing a metallic magnetic material like Fe, Co or Ni is done by means of an evaporator. The design is very simple making the evaporator robust and reliable, see Fig. 4.1. It consists of an exchangeable rod of ultra pure metal (99.99+%) which is biased at high voltage, U, typically 1-1.2 kV.[33] Two thin tungsten filaments are positioned on opposite sides of the pure metal rod and resistively heated at high temperature to emit electrons which are accelerated onto the metal rod, by means of the voltage applied. The induced emission current, I, enables us to regulate the heating power, since the rod temperature is dependent on the power carried by the electrons bombarding the metal rod. This gives the possibility to control the evaporation rate. Another way to monitor the evaporation rate which is external, requires a Quartz Crystal Microbalance (QCM). A QCM measures the deposited mass on the quartz crystal by measuring the change in frequency of a resonator circuit incorporating the quartz crystal. Important when evaporating is, that there are no contaminations on the purified metal rod used in the evaporator and that the pressure is as low as possible in particular during evaporation. In our case the pressure was always $< 10^{-9}$ mbar during evaporation. This is to make sure that the

sample doesn't get unwanted impurities incorporated during evaporation and to reduce the probability of existing rest gases in the chamber to adsorb on the sample. Before evaporation the ultra pure rod undergoes several degassing cycles where it is left under evaporation temperature for longer periods. The low Z impurities being more mobile than the heavier atoms of the material itself diffuse much faster to the surface of the rod and one obtains a much higher degree of purity to start with. Shadow evaporation of a magnetic material onto specially faceted nanostructured arrays of microscopic pyramids as discussed here allows for the fabrication of nanomagnet arrays and the study of their magnetic properties. This technique is applied with evaporation under grazing incidence along the surface, where the grazing incidence shadow deposition results in the deposition of selected facets only. In our case only one facet of a microscopic pyramid is covered, for example, depending on the azimuthal orientation between the metal atom beam and the surface.

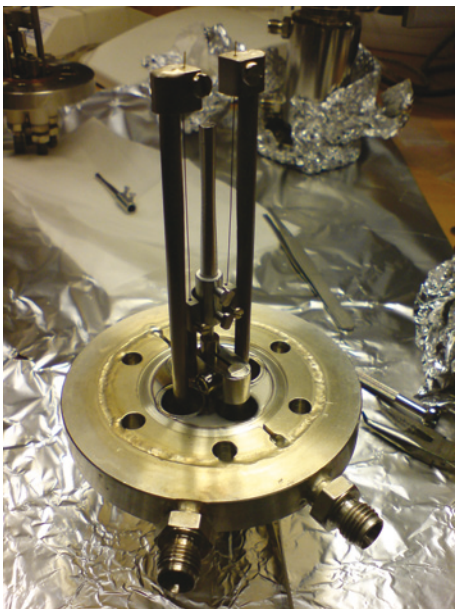

Figure 4.1: Picture of the custom made electron bombardment evaporators used for evaporation of 3*d* metal films. The metal rod seen in the middle is put on positive high voltage and is then bombarded by the emitted electrons from the thin W wires. The W wires are on a symmetric arrangement guaranteeing the mechanical alignment at high temperatures for the rod, close to melting point. When mounted in UHV the evaporator is surrounded by a water cooled shroud. The UHV flange, where the evaporator is mounted is also water cooled.

4.3 Formation and characterization of magnetic nano dot arrays

Prior to evaporation in UHV the substrates were characterized *in situ* by means of atomic force microscope (AFM). AFM is a possibly single atom resolution type of scanning probe microscope. Here we use it at lower than atomic lateral resolution, as the pyramids have a lateral size of order 100 nm. AFM enables studies of nanotechnology and manufacturing of nanometer scale devices. AFM imaging, results from scanning a tip over a surface, using one of the so called primary modes of operation. Here one probes the forces acting on the tip, while the tip is executing different types of motion very close to the surface.[34]

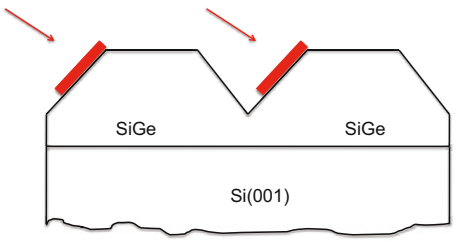

Figure 4.2: The figure schematically illustrates the principle of shadow deposition on a self organized surface. A regular array of Mayan pyramids is observed when a SiGe film is grown on the Si(001) surface under specific conditions. A beam of Co atoms is evaporated under a grazing incidence angle. As a result the Co is covering only one of the pyramid faces.

Creating large areas of nanostructured surfaces can be done in different ways, one elegant approach to get nanostructured arrays is by self organization. The atoms spontaneously arrange themselves, they self-organize, in rather uniform aggregates forming large areas of nanopatterns on the surface. This phenomena can be observed at the surface during epitaxial growth or by means of ion bombardment on some surfaces. The result with epitaxial growth can be divided into two different categories, one dimensional (1D) ripple structures and two dimensional (2D) nanostructured arrays. Here we focus on SiGe self organized pyramid arrays on the Si(001) surface. The existence of a regular array of pyramids for this system is due to strain release upon the growth of the SiGe film. Fig. 4.2 illustrates schematically SiGe Mayan pyramids on a Si substrate. In the presence of lattice mismatch, strain builds up during hetero-epitaxial growth because the film starts to grow with the lattice constant of the substrate. As a consequence the growth is influenced by strain relaxation mechanisms. For the case of Ge/Si one has to deal with compressive strain, as the Ge lattice constant is 4.2 % larger than that of Si. In the early stage of growth, for Ge or SiGe alloys on Si(001) the strain relief mechanisms during growth have been characterized. At low thickness strain can be

vertically relieved by tetragonal distortion. At higher thickness lateral strain is relieved by surface reconstruction.

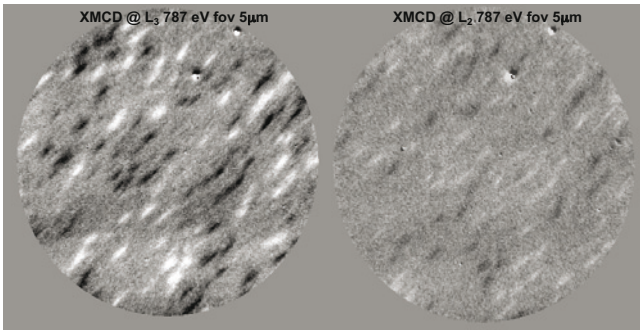

Figure 4.3: XMCD-PEEM micrographs taken at the nano spectroscopy BL at Elettra. *Left panel*: XMCD at the L_3 edge (787 eV) Field of View (FOV) 5 μm *Right panel*: XMCD at the L_2 edge (802 eV) FOV 5 μm for Co/Pt dots, for the name sample area. The azimuthal direction of evaporation is at 45° to the horizontal. The x-rays are incident along the horizontal direction, and at grazing incidence to the surface. Only the in-plane magnetized dots are seen in this geometry. The magnetic contrast difference micrograph shows here, indicate magnetic dots at 300 K. As the photon energy is changed the magnetic contrast is reversed as expected. We observe that the dots point in two different directions in the plane. The dots are elongated perpendicular to the evaporation direction. The gray areas where no XMCD contrast is seen, are most probably out of plane magnetic regions.

As the thickness of SiGe further increases one observes coherently strained crystallites. Also dislocated crystallites can be observed, being fully relaxed on the top. Self organized surface patterns can be observed in all stages of growth. In the substrates used here, one observe self-organization in the form of a regular network of pyramids. The self organization is attributed to strain mediation through the Si layer causing not only a lateral but also a 3D self organization of the crystallites. This effect is rather general and has also been observed for many semiconductor surfaces. The exposed layer of the surface finally terminates in an amorphous SiO thin layer. The Co is shadow deposited on this oxide layer on top of the SiGe pyramids, as is shown in Fig. 4.2.[35] The existence of isolated Co dots can be probed by an element specific technique such as PEEM, see Fig. 4.3, the existence of isolated Co dots and their magnetic properties can be probed, see section 3.3. The self organization approach has its disadvantages compared to other methods, for example offers less control on structure, shape and size. However, for nano technology applications where homogenous formation over macroscopic distances is more important than very exact structure, shape and size of the individual nano objects, self organization has the advantage of the large scale arrays of nanostructures that can be cheaply made, which can directly be used for large scale production.

5. Nano dot arrays on $Si_{0.5}Ge_{0.5}$: Au/Co/Au and Pt/Co/Pt

5.1 Au/Co/Au on $Si_{0.5}Ge_{0.5}$ (Paper II)

Here is given a short summary of some of the results of this Thesis. Fig. 5.1 (a) and (b) present the dependence of both the effective spin moment and the ratio of the orbital- to the effective spin-moment for Au/Co/Au. The solid (open) symbols indicate the values of out of plane (in plane) moments. As can be seen the measurements were done at both 100 K (squares) and 300 K (circles). It can be observed that the deposition of Co and Au influence differently the effective spin moment value and the orbital to spin moment ratio. Both the spin moment and the orbital moment scale to the amount of remanent magnetization, therefore the orbital to spin moment ratio is independent from it. Here, using BL D1011 at MAX-lab, given the macroscopic beam spot size (of order 1 mm^2) we probe the existence of a macroscopic magnetic remanence, in contrast to the XMCD-PEEM results on these samples, where one resolves individual magnetic dots. The stable macroscopic remanence increases with Co deposition onto the Au buffer layer, both at 100 K and 300 K. When the Co layer thickness increases to 4.9 Å the effective in plane spin moment almost reaches 100 % of of the macroscopic remanence. The out-of-plane value, in comparison, reaches only about 10 % of the total remanence. The predominance of in plane alignment at the expense of the perpendicular alignment seen in the figure illustrates that for this Au/Co/Au system we are still in the spin reorientation transition region. For the equivalent thickness for thin films one expects at 100 K a stable out of plane macroscopic remanence. These results are in agreement with the XMCD-PEEM results taken on these samples. We observe using XMCD-PEEM that a multi-domain magnetic state is found at 300 K, therefore a reduced macroscopic magnetic remanence is expected.

With an additional deposition of 3 Å of Au on top of the (4.9 Å)Co/(10 Å)Au the in-plane component of the effective spin moment at 100 K remains almost constant. However, the in plane component at 300 K increases up to 35 %. A further increase of the Au capping should, in principle, lead to an increase of the dot's magnetocrystalline anisotropy. As a strong magnetocrystalline anisotropy favors a single domain state in thin films one should see an increase in the out of plane response at the expense of the in plane one. However, the low values which are still obtained, indicate that the out of plane

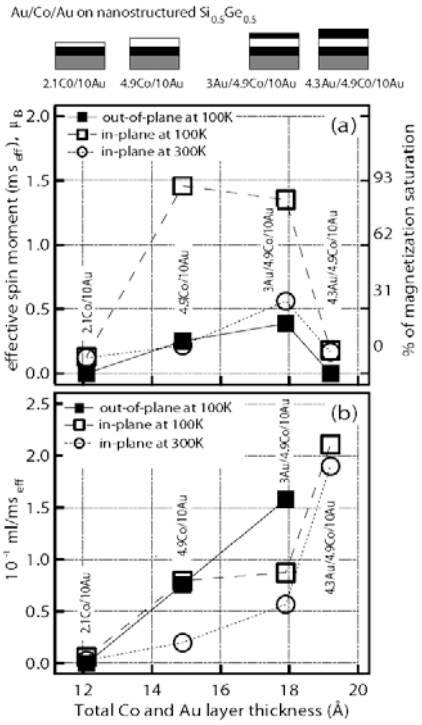

Figure 5.1: The XMCD sum rule analysis results are summarized here versus Co and Au thickness. The data are taken in the magnetic remanent state. Values of spin (a), and orbital to spin moment ratio (b), derived from XMCD measurements performed at remanence on different (Co/Au)-based structures grown on self-organized $Si_{0.5}Ge_{0.5}$ substrates at 300 K. Filled and open symbols are for out-of-plane and in-plane magnetic moments, respectively.

remanent magnetization component breaks up into domains with alternating up-down orientations.

In Fig. 5.1 (b), the variation of orbital- to spin-moment ratio is shown. This ratio is independent of the magnetic remanence value. Any strong changes of this ratio can be correlated with variations of the orbital moment, due to the fact that changes in the spin moment are of order typically up to 10 %. It is remarkable that we observe here variations of order of 100 % for this quantity. Such a strong variation is possible given the increased surface to volume ratio versus a corresponding thin film. It may reflect here variations of the local symmetry around the Co atoms which will lead to strong variations of the orbital moment. It can be seen that the in-plane and out-of-plane orbital- to spin-moment ratio for both 100 K and 300 K, follow initially a linear trend with different slopes as a function of the total Co and Au thickness. It is remarkable that a linear trend can be established versus the total Co and Au thickness, indicating that the local symmetry of the Co atoms is strongly influenced by

means of the Au deposition as well. The values for the ratio for in-plane and out-of-plane at (4.9 Å)Co/(10 Å)Au is the same at 100 K and much higher compared to the in-plane value at 300 K. Also a strong anisotropy for in-plane versus out-of-plane is observed for (3 Å)Au(4.9 Å)Co/(10 Å)Au at 100 K, in contrast to the (4.9 Å)Co/(10 Å)Au case at 100 K. For a given temperature these strong variations can be eventually traced back to structural effects. The fact that also for a constant total thickness a variation of the in plane orbital moment is observed highlights the fact that the spin reorientation transition may be linked to small structural variations for this dot array. *In situ* EXAFS measurements may allow to clarify this point in the future.

5.2 Au/Co/Au vs Pt/Co/Pt on $Si_{0.5}Ge_{0.5}$ (Paper III, I)

Fig. 5.2 (a) and (b) present in detail the effective spin moment and the ratio of the orbital- to the effective spin-moment of Pt/Co/Pt. Solid (open) symbols indicate the values of out-of-plane (in-plane) moments. From Fig. 5.2 we see that the overall macroscopic remanence for the spin- and the ratio of orbital- to spin-moment is minimal at 100 K, by the evaporation of a couple of monolayers of Co on Pt. The evaporation of more Pt partly favors the in-plane remanent magnetization on the

expense of the out of plane magnetization, reaching a maximum for the out of plane remanence at (5.5 Å) Pt/(2 Å) Co/(2 Å) Pt. Even with further deposition of both Co and Pt it was not possible to rotate the moments to out-of-plane at a macroscopic length scale, indicating that the thickness range for an out of plane macroscopic magnetic moment is very narrow and that a multi-domain state is always present. At 300 K we couldn't observe a stable out-of-plane macroscopic magnetic moment in remanence. The orbital- to spin-moment ratio, is here varying much less than for Au/Co/Au and more close to the Co bulk value (0.095). Given the results of Fig. 5.1 and Fig. 5.2 for the Au/Co/Au and Pt/Co/Pt dot systems an anisotropy of the orbital moment is not always linked with the existence of a spin reorientation and does not necessarily follow the so called Bruno model.[5] For the Au/Co/Au dot arrays both scenarios were observed as a function of Au cap thickness. The difference observed for the orbital moment between the two systems indicates that also structural differences exist between the two systems, as the orbital moment is strongly dependent upon the local symmetry around the Co atoms and varies differently for the Co/Pt and Co/Au dot arrays. The data of Table 5.1 indicate measurable differences between the two systems for the last point of each series probed by Co K-edge EXAFS, the most striking difference being the observation of two distinct Co-Co first neighbor shells for the Au/Co/Au dot case, versus a single Co-Co first neighbor shell for the Pt/Co/Pt case.

We observe that in both cases the number of neighbors is reduced by about 50 %, confirming that in both cases one deals with ultra thin Co dots, a re-

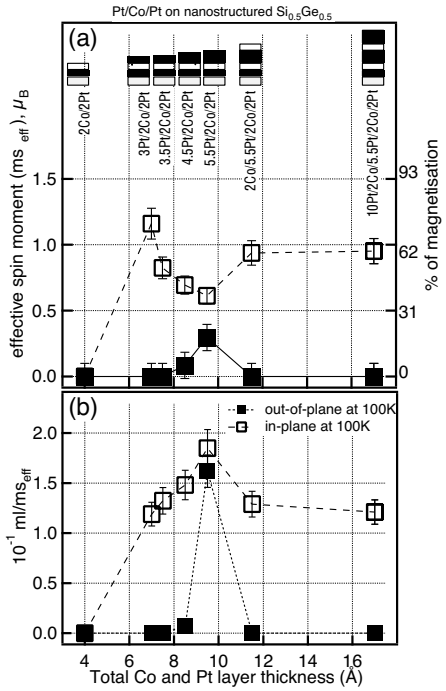

Figure 5.2: Data taken in the magnetic remanent state. The XMCD sum rule analysis results are summarized here versus Co and Pt thickness. Values of spin (a), and orbital to spin moment ratio (b), derived from XMCD measurements performed at remanence on different (Co/Pt)-based structures grown on self-organized $Si_{0.5}Ge_{0.5}$ substrates at 300 K. Filled and open symbols are for out-of-plane and in-plane magnetic moments, respectively.

sult also found for Co on a Au(111) surface. The amount of disorder (Mean Square Relative Displacement (MSRD) factor) is also different between the two systems. The existence of two shells, allows in the case of Au to have a lower amount of disorder for each shell. For the Co/Pt dots, the nearest neighbor shell distance is found to be very close to Co bulk value. The orbital moment does not exhibit an anisotropy for Co/Pt. One obtains a much more pronounced macroscopic perpendicular remanence (Fig. 5.2) when a stronger deviation of the local structure is observed relative to the bulk, such as for Co/Au, a stronger variation of the orbital moment is then observed (Fig. 5.1). One observes that the range of stability of the perpendicular phase of the magnetization is larger for Co/Au. It can be concluded that the magnetic properties at the macroscopic level are mirrored at the local atomic environment characterized by EXAFS at the level of the Co-Co nearest neighbor distance. From the present set of data it is not possible to identify any Co-Au or Co-Pt distance back scattering contribution to the EXAFS. Always a good fit was produced

Table 5.1: *Co-Co nearest two shell distances, corresponding coordination numbers, N^*, and Mean Square Relative Displacement (MSRD) factors for the Pt/Co/Pt, Au/Co/Au nano dot arrays on nano structured $Si_{0.5}Ge_{0.5}$. The parameters resulting from the analysis of the data of the Co foil, measured and analyzed under identical conditions is also shown. The Au/Co/Au data have also been discussed earlier. The Co foil data can be fitted with the Co bulk structural parameters. Two Co close lying shells are identified for Au/Co/Au. For Pt/Co/Pt only one neighbor shell is found. Only Co neighbors were identified within the first FT peak analyzed here.*

	Co foil	Au/Co/Au	Pt/Co/Pt
R_1(Å)	2.49(1)	2.47(2)	2.50(2)
R_2(Å)	2.51(1)	2.59(2)	-
N_1^*	6.0(5)	4.0(5)	6.0 (10)
N_2^*	6.0(5)	3.0(5)	-
σ_1^2 (Å^2)	0.0030(5)	0.0050(5)	0.0070(5)
σ_2^2 (Å^2)	0.0030(5)	0.0050(5)	-

for the experiments including only the electron scattering from the Co atoms. The fit was produced using calculations from the FEFF code in combination with the *Athena* and *Artemis* programs.[36][37] This is consistent with the bulk type of distance obtained for the first Co neighbors in both cases. The growth of the Co on both Au and Pt on SiGe appears to be incoherent. One would expect a distance of order 2.8-2.9 Å if the growth would be coherent. The amount of disorder is expected to be much higher for the Co-Au and Co-Pt distances, reducing there EXAFS below the noise level.

5.3 Outlook: Future work on nano dot arrays

The results presented in this Thesis demonstrates that by means of *in situ* surface science combined with shadow evaporation one can control the shape and composition of magnetic nano dot arrays. XMCD-PEEM appears to be an instrument of choice, allowing even to visualize the magnetic orientation of single magnetic dots at room temperature. The XMCD technique in the XAS mode, appears to be sensitive enough to characterize the orbital moment of these very dilute samples in terms of magnetic material. As a dipole magnet x-ray source is used here, we have been able to characterize a rather large assembly of magnetic nano dots. With brighter circular x-ray light one should attempt to measure the orbital moment in a much smaller area of the surface if possible comprising only a few dots only. This may be possible at MAX-lab in the near future, using undulator radiation, at the I1011 beamline.

The work presented here reveals, furthermore, by means of the Co-Co distances structural distortions for the Au/Co/Au system but not Pt/Co/Pt. This finding appears to be correlated to the overall value and anisotropy of the Co orbital moment. Trying to stabilize the out of plane response and obtain individually addressable out of plane dots, the local structure appears to play also a role for dot arrays not only the dot size or shape. Certainly more studies are needed as a function of dot size, Co and cap layer thickness.

The EXAFS results indicate that the Co must be in a more relaxed state when grown in dots together with Pt, since the Co-Co distances are similar to those found in the hcp Co foil, and also indirectly by the invariance observed in the magnetic moment with increasing Pt capping. With Au, on the contrary, a more marked evolution of the magnetism with both Co and Au thicknesses is observed. One can speculate here of a stronger Co-Au interaction, a surprising result, given the filling of the outermost d shells one would in principle expect the opposite. The results on the spin reorientation transition indicate that the magnetic properties in the dot systems are very different from those observed in two dimensional films and multilayers. The present work clearly highlights with the spectroscopy tools put forward that the study of magnetic nano dot arrays is an interesting, if challenging topic, worth continuing. One can for example now vary the size of the islands or the shape of the nano objects and repeat some of these studies, trying to probe the influence of the dots shape and surface to volume ratio on the magnetic properties.

6. Exchange Bias and Frozen Spins

6.1 The NiFe/FeMn exchange bias system (Paper V)

Pinned or frozen magnetic moments are studied within an exchange biased NiFe ferromagnet at the NiFe/FeMn ferromagnet/ anti-ferromagnet interface by magnetic circular dichroism in x-ray absorption and resonant reflectivity experiments. Frozen moments are detected by means of the element specific hysteresis loops. Also a weak dichroic signal in absorption of unidirectional symmetry can be correlated to frozen magnetic moments in the ferromagnet. The NiFe/FeMn system is chosen as it constitutes a high temperature EB system, experiments are possible at 300 K.

The Ni frozen moments are measured by XMCD for variable layer thickness of the AFM by directly detecting the FM interface specific to Ni moments, using geometries shown in Fig. 6.1. This is achieved by the precise choice of the thickness of the AFM and the capping layer in the electron yield mode in combination with the complete study of the angular dependence of the XMCD signal. This leads to the characterization of the frozen Ni moments in terms of both the orbital and spin moments per atom. Standard XMCD measurements geometries 1 and 2 are used, using magnetization reversal as for a FM. The circularly polarized x-rays are kept at a fixed helicity and are incident on the sample at an angle of 45° with the magnetic field being applied using a pair of Helmholtz coils. The direction of the homogeneous magnetic field is indicated by the two arrow arrays in Fig. 6.1. Using 1 and 2 in remanence after proper normalization and subtraction yield the XMCD signal shown in Fig. 6.1 for the Ni L-edges, no contribution is expected from the AFM part of the sample or the frozen spin moments. By turning the sample 90° as compared to the previous cases, and using geometries 3 and 4 in Fig. 6.1 it is possible to measure the frozen moments, since the frozen moments are now either parallel or anti parallel to the incident x-rays. A more pronounced exchange bias for increasing thickness of the FeMn layer correlates with an increase in orbital moment for interface Ni atoms carrying a pinned or frozen magnetic moment. These results complement previous XMCD work for EB systems, as the pinned or frozen spins are traced here on the ferromagnet side. This work also extends previous results, as the accuracy of the present analysis allows also for the determination of the orbital part of the magnetic moment.

For the Element Specific Magnetic Hysteresis (ESMH) loops measurement, see Fig. 6.2, we also rely on the geometry presented in Fig. 6.1, but now at grazing x-ray incidence angles at plus and minus 7°. Combining the results

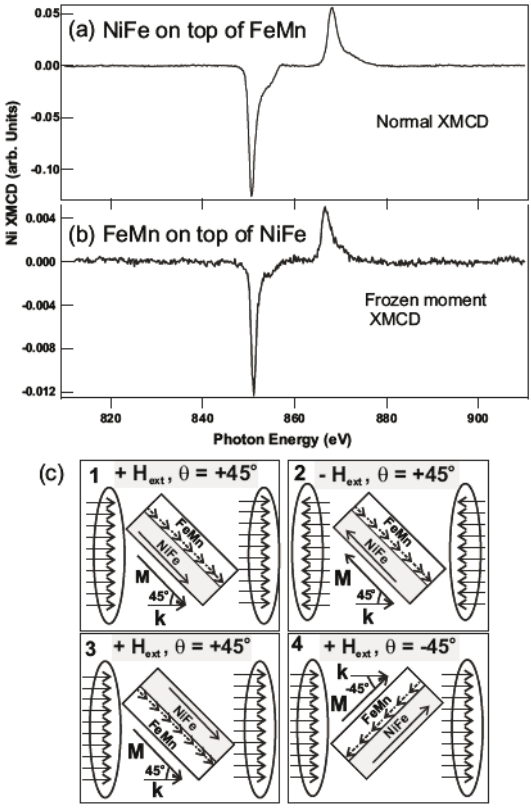

Figure 6.1: (a) Normal Ni XMCD signal for NiFe on top, whereas (b) represents the frozen Ni signal with the FeMn on top, for 7 nm FeMn and 5 nm NiFe layers. Insets on (a) and (b) present the geometries used for the measurements. The light helicity is kept constant. The incident x-ray direction is denoted by the **k** vector, the x-rays were incident at an angle of 45° from the sample surface. Parallel arrows indicate the direction of the applied field, the single arrow on the FM (ferromagnet) denotes the orientation of the magnetization within the FM following the applied field. Dotted arrows show the interface pinned spins.

from XMCD and ESMH, it yields that for Fe only when the EB effect is stronger, as in the right figure panel, one can clearly observe Fe frozen moments in the form of a vertical shift in the loop. For this sample with a thicker FeMn layer, presented in the right hand panels in Fig. 6.2, we see a larger horizontal shift of the Fe hysteresis loops correlating with a stronger EB field. Together with this horizontal shift one clearly observes the vertical shifts for both the Fe and Ni edges. In conclusion the larger vertical ESMH shift observed at the Ni edge for the sample with the thinner FeMn layer, does not correlate with the smaller EB effect in this case, indicating that all the frozen moments do not necessarily contribute equally to the EB effect.

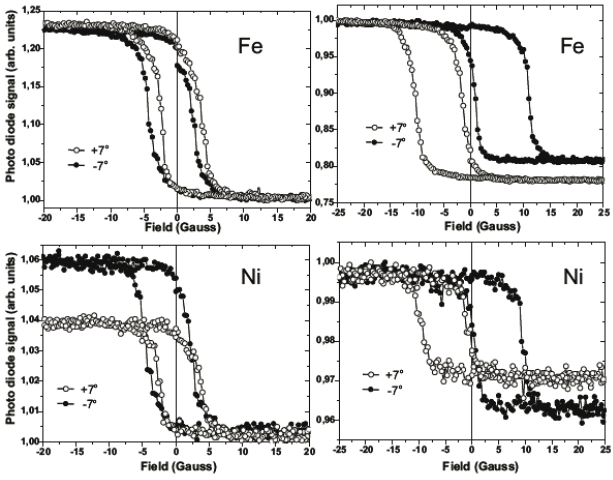

Figure 6.2: Hysteresis loops for Fe edge (top) and Ni edge (bottom) at grazing incidence (+ and - 7°) for sample with NiFe (5 nm)/FeMn (7 nm) for the left column and NiFe (5 nm)/FeMn (9 nm) for the right. The two hysteresis loops in each panel were taken with the EB field direction parallel and anti-parallel to the incident x-rays.

7. Correlating magnetism and structure

7.1 L-edge EXAFS: Au/Co/Au/W(110) (Paper IV)

In the soft x-ray regime the analysis of EXAFS data faces substantial difficulties due to overlapping L-edges and background anomalies due to, multiple electron excitation, atomic EXAFS and eventually systematic experimental errors.[38] However, the advantageous information that is available in L-edge EXAFS compared to K-edge EXAFS makes this technique worthwhile trying, due to the extreme fragility of most *in situ* samples. Uncapped samples of 3d-transition metals, for example, if taken outside of the chamber have a very high probability of being contaminated and thus change the magnetic properties of the sample. Therefore L-edge EXAFS is advantageous, since the sample can remain in the chamber. Soft x-ray L-edge EXAFS gives *in situ* information on the correlation between structure and magnetism for the of 3d-transition metals. Small structural distortions have a great influence on the magnetic anisotropy.

The magnetic anisotropy of a magnet is governed by the shape anisotropy and the magnetocrystalline anisotropy. The shape anisotropy depends on the geometrical shape of the sample, the magnetocrystalline anisotropy depends on the orientation of the magnetization relative to the crystal lattice. As pointed out earlier, given the difference in local symmetry, electronic structure and crystal structure, in an ultra thin film the interface atoms yield a contribution to the magnetocrystalline anisotropy different than the inner film layers. In the case studied here for the Au/Co and Pt/Co interfaces, the interface atoms favor an out of plane easy direction. Here the system Au/Co/Au was investigated in thin film form as well as in the form of dot arrays on a self organized surface. It is found that in some cases the orientation of the magnetization can deviate from the expected out of plane direction, also in the ultra thin limit. For the system Au/Co/Au grown and characterized *in situ* on a W(110) surface in combination with the characterization of the magnetization orientation by means of XMCD, Co L-edge Extended X-ray Absorption Fine Structure (EXAFS) measurements were performed to study the local structural changes as the Co films were grown, *in situ*, step by step, on Au/W(110).

In thin films, in general and for the Co films studied here in particular, the shape anisotropy favors an in-plane direction of the magnetization. Typically for Co/Au the magnetocrystalline anisotropy energy favors the out of plane direction. The magnetic easy axis is determined by the competition between

the shape anisotropy and the magnetocrystalline anisotropy. However, the latter is often enhanced at surfaces and interfaces. When the film is very thin the surface and interface contribution to the magnetic anisotropy energy can dominate and it is possible to obtain a Perpendicular Magnetic Anisotropy (PMA) system. Often a spin reorientation is observed in such a system as a function of Co thickness and temperature. Au/Co/Au is a known as a prototypical system which exhibits PMA. We performed *in situ* Co L-edge EXAFS measurements to study the local structural changes of a 5 Å thick Co film on Au/W(111), as it undergoes the spin reorientation from in- to out-of-plane reorientation, upon capping with a 3.5 Å thick Au film. Interestingly, for this Co/Au interface, an in plane magnetization is observed without a Au cap. The EXAFS measurements were then analyzed by means of the newly introduced in the literature, Bayes-Turchin approach, fine tuned for use in the L-edge EXAFS data analysis.[39][40] Due to the existence of the overlapping L-edges the analysis of the L-edge EXAFS for 3d materials is more challenging than for example, Co K-edge EXAFS also performed, where one deals with the EXAFS contribution from a single edge only.[41] Using the Bayes-Turchin approach it was possible to obtain quantitative information on the structural strain and disorder of the Co layers. The structural information gained points to the fact that the lattice of an in-plane magnetically oriented bare, with no Au cap, 5 Å thick Co film on Au/W(110) is expanded in the in in-plane direction and shrinks in the perpendicular direction, as compared to the Co bulk. Upon capping with a 3.5 Å thick Au film, this Co film undergoes a spin reorientation and exhibits an out-of-plane magnetization. The L-edge EXAFS indicates that this reorientation is correlated to a lattice expansion in the perpendicular direction. Compared with the bare 5 Å thin Co film upon capping, we observe structural changes of the lattice parameters in the surface plane, a, and out of plane, c, of $\Delta a/a = 1.2\%$ and $\Delta c/c = +6.6\%$ which leads to a total increase of the volume of the Co unit cell by 4 % as compared this time with the hcp like Co bulk film. This finding indicates a strong correlation between structure and magnetism for the Co/Au interface. The anomalous, for Co/Au, easy in plane direction can be discussed in terms of a magneto elastic energy contribution for the Co/Au interface. With the help of the XMCD results yielding the magnetic easy direction and the EXAFS results yielding the local structural distortions, a quantitate determination of magneto-elastic constant of these films were determined. These thin film results open up the possibility for a better understanding of the results in the case of Au/Co/Au nano dot arrays on SiGe. Much like in the present case of the 5 Å thick Co film on Au/W(111), where a small quantity of Au has strong effects on the magnetic properties, also for the Co/Au and Au/Co/Au dot arrays, small additions of Au in the sub monolayer range have strong effects in the orbital moment anisotropy and the easy magnetization direction.

8. Structural and magnetic properties of MnSb

8.1 XMCD and EXAFS on molecular beam epitaxy grown MnSb layers on GaAs substrates (Paper VII)

To tailor the magnetic properties of semiconductor materials, inclusions in the nanometer range are incorporated in the semiconductor lattice. In order to obtain materials with the desired magnetic properties to form ferromagnetic nano inclusions, it is reasonable to start with a magnetic material, suitable for incorporation in a semiconductor, with a Curie temperature above room temperature. A good candidate to be incorporated in GaAs is MnSb, it has been shown that the Curie temperature of MnSb in the bulk is 587 K and that $Mn_{1-x}Sb_x$ layers grown on GaAs reach a Curie temperature of 620 K. The latter results provide a good indication that MnSb may form stable ferromagnetic nano inclusions, leading to ferromagnetism above room temperature. As a first step in such a program one studies MnSb layers grown on GaAs.

For the studies of the present work, MnSb thin layers were grown on two types of substrates: GaAs(111) and GaAs(100) by Molecular Beam Epitaxy (MBE) in Ultra High Vacuum (UHV). The samples were then characterized using X-ray Absorption Near Edge Structure (XANES) and Extended X-ray Absorption Fine Structure (EXAFS) at the Mn K-edge. The results are compared with MnSb powder used as a reference, measured *in situ* under the same experimental conditions. The EXAFS analysis yields that the local structure around Mn atoms is similar for both investigated samples and close to the one of the powdered MnSb. In particular, the amount of structural disorder is found to be the same in both cases indicating a rather disordered structure for the thin MnSb layers on GaAs.

Hysteresis loops were measured by means of Superconducting Quantum Interference Device (SQUID) magnetometry, to gain some information on the magnetic properties of MnSb on GaAs(111) and GaAs(100). One characterizes here the magnetic properties of the whole MnSb film. The magnetization for MnSb on GaAs(111) was found practically saturated at 250 Gauss at both 300 K and 100 K. MnSb on GaAs(100) on the other hand, had a higher magnetization saturation at a field of 1000 Gauss at booth 300 K and 100 K. Both samples show a weak coercivity and a rather fast response to the applied magnetic field, indicating a strong ferromagnetic coupling between the Mn ions.

The X-ray Magnetic Circular Dichroism (XMCD) measurements were performed at beam line D1011 at MAX-lab. The XMCD spectra were taken in

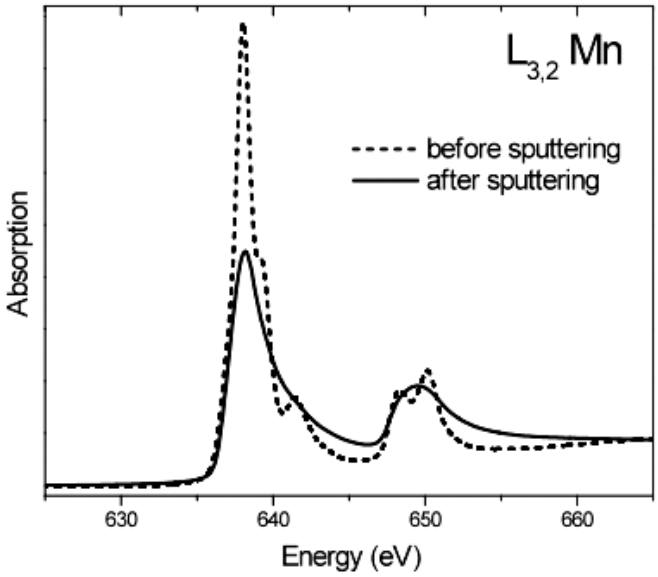

Figure 8.1: The spectral region around the Mn L_3 and L_2 edges is shown in some detail. The fine structure before sputtering is characteristic of the presence of oxygen as a nearest neighbor to the Mn atoms. As the oxygen atoms are removed by sputtering the number of 3d empty states of the Mn atoms decreases and the white line intensity is reduced. The white lines become also broader, mirroring the more delocalized nature of the 3d states close to the Fermi level.

the electron yield mode, a technique probing the near surface region of the MnSb films, some 5nm only, a very small fraction of the total thickness which is of order 200 nm. The samples were studied in an *ex situ* mode. They were exposed to air to be introduced to the D1011 UHV chamber for the XMCD measurements. Given the exposure to air, for the samples as introduced from air, MnSb in the near surface region is found to contain oxygen, a layer which has to be removed to be able to analyze the XMCD measurements. The fact that oxidic features are seen at the Mn L-edge see Fig. 8.1, is indicative that oxygen atoms are nearest neighbors to the Mn atoms and the presence of oxygen in the near surface region can be monitored at both the oxygen and the manganese L-edges. The oxygen could be removed by ion sputtering. When all the oxygen is removed the Mn spectra get a metallic look, highlighting a more delocalized character of the 3d final unoccupied states and all the white line satellites are quenched. Comparing the x-ray absorption spectra before versus after sputtering, one observes that the spectral intensity of the white lines decreases and the inter-peak region increases as the oxygen amount is reduced. Fewer unoccupied Mn 3d final states are available after sputtering, the high L edge inter-peak continuum indicating the delocalized character of

the final states at the corresponding energy range above the L_3 white line maximum energy.

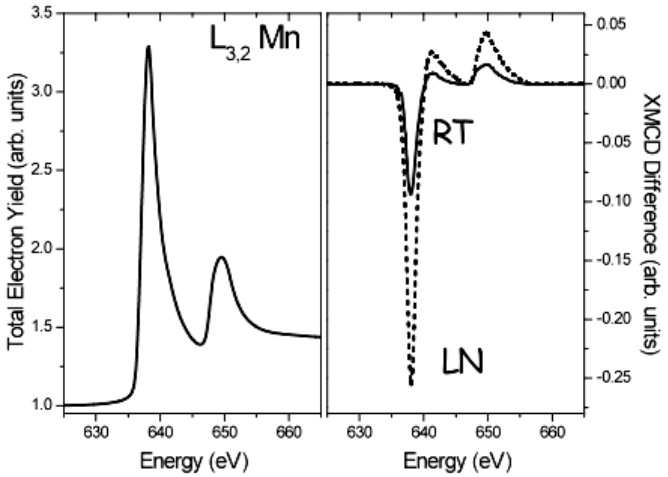

Figure 8.2: Absorption spectrum (left) and corresponding XMCD of the MnSb on GaAs (111) sample recorded at 300 K and 100 K (right). We observe an increase of XMCD intensity between these two temperatures, indicative of the fact that the near surface region does not exhibit the bulk like magnetic properties.

An important information x-ray absorption provides here that can lead to a quantitative information in terms of ground state electronic structure, is the number of the 3d holes localized around the Mn sites. A decreasing white line intensity in this case points out that the Mn electrons are transferred to oxygen in the oxidic state, thus increasing the number 3d holes at the Mn sites. After sputtering, the oxygen atoms are removed and the 3d electrons are transferred back to the Mn sites, thus decreasing the number of 3d holes, as compared to the state of the sample before sputtering. Once the sample was oxygen free, the magnetic moments were obtained by a direct application of the magneto optical sum rules in the magnetic remanent state. The magnetic moments in remanence are substantially smaller than the saturation values reported in the literature. One possibility to explain this effect is the existence of closure domains at the near surface region, such domains will drastically reduce the remanent magnetic moments. One observes an increase in magnetic remanence upon cooling the sample from 300 to 100 K, see Fig. 8.2. It is not clear if this effect is due to a reduction of the Curie temperature or possibly a variation of the magnetic domain structure in the near surface region. A comparison with the SQUID data, indicate drastically different magnetic properties for the near surface region as compared to the MnSb bulk for the samples studied. This result is confirmed by the study of the orbital moment in the remanent state. By applying the magneto optic sum rules, also the orbital

contribution to the magnetic moment can be obtained for the Mn atoms. An enhanced value is obtained versus theoretical calculations. This result can be explained by means of the enhanced surface to volume ratio for the samples studied. Surface Mn atoms, are expected to yield an enhanced orbital moment due the reduced local symmetry, leading to a lifting of the quenching of the orbital moment in a high symmetry configuration. Such enhancement effects of the orbital magnetism are commonly seen for metallic surfaces or for nano structures. The AFM and electron microscopy measurements indicate the existence of many voids, leading to the existence also of an internal surface. The layers appear to consist of an assembly of columnar MnSb crystallites in the micron range. Here one can argue on one hand that the material grown is of poor crystalline quality within a long range crystallographic perspective. On the other hand, the magnetic anisotropy is governed by means of the orbital moment anisotropy more sensitive to the short range order and local symmetry probed by x-ray absorption and XMCD. The present results may indicate an efficient way to manipulate the magnetic anisotropy by enhancing the orbital moment, and stabilize ferromagnetic order at even higher temperatures for this family of magnetic materials.

Acknowledgements

I would like to thank you Dimitri for all the support, encouragement and understanding. Thank you Jonathan and Charlie for your help. Nils and Svante, thank you. Your support and encouragement are appreciated. I am grateful to the staff at MAX-lab and colleagues at the Department for their support. Thank you Juanjo for your hospitality in Madrid and your constant support. Thank you Miguel, Jyoti and Iwona for keeping up at MAX-lab during the long measurements. Lidia, your presence, within our small group at MAX-lab, made always life brighter. Elisabeth, I always enjoyed our join work at MAX-lab, thank you for your support and hospitality in Berlin, extending well beyond life in the Institute. Masako, and Konishi-san, thank you for all the discussions we had and our join work. Ania thank you for your hospitality in Warsaw, our beam times have been hard work, always with some chocolate in the end of the tunnel, making life more enjoyable.

Last but not least, I want to thank my family and friends that have helped me and supported me during this period.

Uppsala, 25 January, 2010

Andreas Persson

Bibliography

[1] Sushin Chikazumi. *Physics of Magnetism*. John Wiley & Sons. Inc., 1978.

[2] David Jiles. *Introduction to MAGNETISM and MAGNETIC MATERIALS*. Chapman & Hall, 1991.

[3] J.A.C Bland B. Heinrich. *Ultrathin Magnetic Structures I*. Springer-Verlag Berlin Heidelberg New York London Paris Tokyo Hong Kong Barcelona Budapest, 1994.

[4] Mathias Getzlaff. *Fundamentals of Magnetism*. Springer-Verlag Berlin Heidelberg New York London, 2008.

[5] P. Bruno. *Chapter 24, 24. IFF-Ferienkurs, Magnetismus von Festkörpern und Grenzflächen*. Forschungszentrum Jülich, 1993.

[6] Amikam Aharoni. *Introduction to the Theory of Ferromagnetism*. Oxford University Press Inc., 2000.

[7] W.H. Meiklejohn and C.P. Bean. *Physical Review*, 102(5):1413 – 1414, 1956/06/01.

[8] H. Ohldag, T.J. Regan, J. Stohr, A. Scholl, F. Nolting, J. Luning, C. Stamm, S. Anders, and R.L. White. *Physical Review Letters*, 87(24):247201 – 1, 2001/12/10.

[9] H. Ohno, F. Matsukura, and Y. Ohno. *JSAP International*, (5), 2002/01/.

[10] T. Dietl, H. Ohno, F. Matsukura, J. Cibert, and D. Ferrand. *Science*, 287(5455):1019 – 22, 2000/02/11.

[11] A. Kimura, S. Suga, T. Shishidou, S. Imada, T. Muro, S.Y. Park, T. Miyahara, T. Kaneko, and T. Kanomata. *Physical Review B (Condensed Matter)*, 56(10):6021 – 30, 1 Sept. 1997.

[12] Jin-Cheng Zheng and J.W. Davenport. *Physical Review B (Condensed Matter and Materials Physics)*, 69(14):144415 – 1, 2004/04/01.

[13] R. Coehoorn and C. Haas. *Physical Review B (Condensed Matter)*, 31(4):1980 – 96, 1985/02/15.

[14] http://www.maxlab.lu.se/beamlines/bld1011/.

[15] D. Arvanitis, M. Tischer, J. Hunter Dunn, F. May, N. Martensson, and K. Baberschke. pages 145 – 57, Berlin, Germany, 1996//.

[16] C.T. Chen, Y.U. Idzerda, H.-J. Lin, N.V. Smith, G. Meigs, E. Chaban, G.H. Ho, E. Pellegrin, and F. Sette. *Physical Review Letters*, 75(1):152 – 5, 1995/07/03.

[17] E. Beaurepaire F. Scheurer G. Krill, J.-P. Kappler (Eds.). *LNP 565, Magnetism and Synchrotron Radiation*. Springer-Verlag.

[18] P. Carra, B.T. Thole, M. Altarelli, and Xindong Wang. *Physical Review Letters*, 70(5):694 – 7, 1993/02/01.

[19] B.T. Thole, Paolo Carra, F. Sette, and G. van der Laan. *Physical Review Letters*, 68(12):1943 – 6, 1992/03/23.

[20] J. Stöhr. *Journal of Magnetism and Magnetic Materials*, 200:470–497, 1999.

[21] P. Soderlind, O. Eriksson, B. Johansson, R.C. Albers, and A.M. Boring. *Physical Review B (Condensed Matter)*, 45(22):12911 – 16, 1992/06/01.

[22] D. Weller, J. Stöhr, R. Nakajima, A. Carl, M. G. Samant, C. Chappert, R. Mégy, P. Beauvillain, P. Veillet, and G. A. Held. *Physical Review Letters*, 75(20):3752–3755, 1995.

[23] R. Wu, D. Wang, and A.J. Freeman. *Physical Review Letters*, 71(21):3581 – 4, 1993/11/22.

[24] Ruqian Wu and A.J. Freeman. *Physical Review Letters*, 73(14):1994 – 7, 1994/10/03.

[25] J. Hunter Dunn, D. Arvanitis, N. Martensson, M. Tischer, F. May, M. Russo, and K. Baberschke. *Journal of Physics: Condensed Matter*, 7(6):1111 – 19, 1995/02/06.

[26] J. Hunter Dunn, A. Hahlin, O. Karis, D. Arvanitis, G. LeBlanc, A. Andersson, and L.-J. Lindgren. *AIP Conf. Proc. (USA)*, (708):65 – 8, 2004.

[27] A. Locatelli, A. Bianco, D. Cocco, S. Cherifi, S. Heun, M. Marsi, M. Pasqualetto, and E. Bauer. *Journal de Physique IV (Proceedings)*, 104:99 – 102, 2003/03/.

[28] S. Carlson, M. Clausen, L. Gridneva, B. Sommarin, and C. Svensson. *J. Synchrotron Radiat. (Denmark)*, 13:359 – 64, Sept. 2006.

[29] K. Attenkofer, L. Tröger, M. Herrmann, and U. Brüggmann. *HASYLAB annual report*, pages 61 – 65, 1998.

[30] E.A. Stern. *Physical Review B (Solid State)*, 10(8):3027 – 37, 1974/10/15.

[31] A.P. Lee and B.J. Pendry. *Physical Review B (Solid State)*, 11(8):2795 – 2811, 1975/04/15.

[32] Boon K. Teo. *EXAFS: Basic Principles and Data Analysis*. Springer-Verlag, 1986.

[33] www.goodfellow.com.

[34] Roland Wiesendanger. *Scanning Probe Microscopy and Spectroscopy*. Cambridge University Press, 1994.

[35] C. Teichert. *Appl. Phys. A, Mater. Sci. Process. (Germany)*, A76(5):653 – 64, 2003/03/.

[36] J.J. Rehr and R.C. Albers. *Reviews of Modern Physics*, 72(3):621 – 54, 2000/07/.

[37] B. Ravel and M. Newville. *Physica Scripta*, 2005(T115):4 pp. –, 2005/01/.

[38] F.W. Lytle, D.E. Sayers, and E.A. Stern. *Physical Review B (Solid State)*, 15(4):2426 – 8, 1977/02/15.

[39] H.J. Krappe and H.H. Rossner. *Physical Review B (Condensed Matter and Materials Physics)*, 66(18):184303 – 1, 2002/11/01.

[40] H.J. Krappe and H.H. Rossner. *Physical Review B (Condensed Matter)*, 61(10):6596 – 610, 2000/03/01.

[41] H.J. Krappe and H.H. Rossner. *Physical Review B (Condensed Matter and Materials Physics)*, 70(10):104102 – 1, 1 Sept. 2004.

Acta Universitatis Upsaliensis

Digital Comprehensive Summaries of Uppsala Dissertations from the Faculty of Science and Technology 710

Editor: The Dean of the Faculty of Science and Technology

A doctoral dissertation from the Faculty of Science and Technology, Uppsala University, is usually a summary of a number of papers. A few copies of the complete dissertation are kept at major Swedish research libraries, while the summary alone is distributed internationally through the series Digital Comprehensive Summaries of Uppsala Dissertations from the Faculty of Science and Technology. (Prior to January, 2005, the series was published under the title "Comprehensive Summaries of Uppsala Dissertations from the Faculty of Science and Technology".)

Distribution: publications.uu.se
urn:nbn:se:uu:diva-112824

ACTA
UNIVERSITATIS
UPSALIENSIS
UPPSALA
2010